



Dislocation dynamics simulation of thermal annealing of a dislocation loop microstructure

A. Breidi*, S.L. Dudarev

UK Atomic Energy Authority, Culham Science Centre, Oxfordshire OX14 3DB, UK



ARTICLE INFO

Article history:

Received 9 March 2021

Revised 31 December 2021

Accepted 20 January 2022

Available online 29 January 2022

Keywords:

Dislocation loops

Dislocation network

Discrete dislocation dynamics

Post-irradiation annealing

Thermal evolution of dislocations

ABSTRACT

Thermal evolution and elevated temperature annealing of the dislocation microstructure of an irradiated metal, represented by an ensemble of elastically interacting interstitial dislocation loops, is explored using discrete dislocation dynamics simulations. The two fundamental microscopic processes driving the evolution of dislocations are the pipe diffusion of atoms along the dislocation lines, giving rise to the dislocation self-climb, and bulk diffusion of vacancies, resulting in the conventional dislocation climb. Simulations show that the coalescence and coarsening of the prismatic dislocation loop microstructure, observed at lower temperatures, is driven primarily by the dislocation self-climb. In tungsten, dislocation self-climb gives rise to a pronounced change in the dislocation loop microstructure at temperatures close to 800 °C, see Ferroni et al. (2015) [1], whereas a similar microstructural transformation of the dislocation network driven by self-climb in α -iron is predicted to occur at ~ 270 °C. Simulations also show that the diffusion of vacancies in the crystal bulk is able to explain the observed annihilation rates of interstitial loops in tungsten.

Crown Copyright © 2022 Published by Elsevier B.V. All rights reserved.

1. Introduction

The development of quantitative predictive models for the thermal evolution of microstructure of heavily irradiated materials is a major scientific challenge in the context of design of fusion and advanced fission power plants. Irradiation of many metals and alloys at relatively low temperatures, below approximately 350 °C for structural steels [2], gives rise to radiation embrittlement. In the intermediate temperature range, materials exposed to irradiation exhibit radiation swelling [3], whereas at even higher temperatures the performance and lifetime of components is limited by thermal and radiation creep [4,5]. The selection of candidate structural materials for fusion applications includes ferritic-martensitic steels, vanadium, titanium, and copper alloys, silicon carbide, and tungsten as a plasma-facing material [6,7].

Irradiation by high-energy neutrons or ions produces high, many orders of magnitude higher than equilibrium, concentrations of self-interstitial and vacancy defects in materials. The populations of defects produced by irradiation include single-atom defects, for examples self-interstitial atoms and vacancies, as well as clusters of defects [8]. If all the self-interstitial defects generated by irradiation were to migrate directly to vacancies, they would

annihilate fully since irradiation always produces vacancy and self-interstitial defects in pairs, and the total numbers of opposite type defects match each other exactly. In reality, self-interstitial and vacancy defects, and clusters of defects generated by irradiation, segregate [8–10]. As a result, self-interstitial and vacancy defects never annihilate completely, and instead form spatially segregated regions containing excess amounts of defects of either type. For example, self-interstitial defects form interstitial dislocation loops and extended dislocation networks, whereas vacancies remain relatively randomly distributed in the bulk of the material [10–12]. In some materials, self-interstitial defects coalesce into small nuclei of Laves phases [13], whereas vacancies form vacancy clusters, vacancy dislocation loops or voids [3,14,15].

The remaining mobile point defects are absorbed by the so-called sinks, for example by the dislocation network or by grain boundaries, or in a thin film geometry these defects migrate to surfaces. The numbers of defects migrating to sinks and those accumulating in the bulk of the material as individual defects or clusters of defects are not the same for vacancies and self-interstitials. The asymmetry, or bias, in the observed behaviour of defects stems from the elasticity effects [16], in particular from the significant difference between the relaxation volumes of vacancy and self-interstitial atom defects [17–19]. The spatial partitioning and clustering of vacancy and self-interstitial defects results in the formation of spatially heterogeneous dislocation and vacancy microstructures observed in materials exposed to irradiation [10].

* Corresponding author.

E-mail addresses: a.breidi@hotmail.com (A. Breidi), sergei.dudarev@ukaea.uk (S.L. Dudarev).

The fact that the formation energy E_f of a self-interstitial atom defect is relatively high [20], for example in tungsten it is close to 10 eV and in iron to 5 eV, shows that the thermal equilibrium concentration of self-interstitial defects, proportional to $\exp(-E_f/k_B T)$, is negligible [21]. The thermal equilibrium concentration of vacancies at ambient conditions is also very low, but can be appreciable at elevated temperatures [22,23]. The many orders of magnitude difference between the negligible equilibrium and high non-equilibrium, induced by irradiation, concentrations of self-interstitial and vacancy defects creates a thermodynamic force that drives the defects from the bulk to the available sinks, for example to the interstitial loops and dislocations, vacancy loops, grain boundaries, and surfaces.

The energy required to dissociate a self-interstitial atom defect from a line dislocation or a mesoscopic dislocation loop is close to the formation energy of the defect [20]. This renders self-interstitial defects effectively locked in dislocations, and encourages the growth of dislocation loops by the absorption of freely migrating self-interstitial defects [24] or by their coalescence with other loops [25].

Simulations and observations show that already at a relatively low exposure to radiation at the level of 0.1 dpa, interaction between dislocation loops gives rise to the formation of an extended dislocation network [10–12,26]. In situ thermal annealing [1] of ion-irradiated tungsten shows that the dislocation network remains largely static and stable below ~ 1000 K. Dislocations start evolving at higher temperatures, in the range from 1073 to 1473 K, where annealing of the dislocation microstructure can be observed on the timescale of one hour or shorter. Also, since the 2 MeV self-ion irradiation of tungsten used in experimental studies [1] induces defects and dislocations only at a relatively shallow depth ≤ 200 nm below the surface, it is desirable to develop a model that would enable extending the analysis of ion irradiation experiments to the bulk conditions representative of the operating environment for structural materials in a fission or fusion reactor.

We develop a computational model based on dislocation dynamics simulations and apply it to the simulation of evolution and annealing of an ensemble of interacting interstitial dislocation loops, where the dynamics of dislocations involves both self-climb and vacancy-mediated climb. The latter is mediated by the absorption of vacancies, which undergo thermally activated diffusion in the bulk of the material, by the dislocations [27,28]. We find that pipe diffusion along the dislocation lines [29], independent of the vacancy atmosphere and responsible for the self-climb of dislocations, accounts for the observed lower-temperature dynamics of coarsening of dislocation loops in tungsten and iron. At the same time, dislocation self-climb appears to be not the only rate-controlling process consistent with the microstructural evolution observed in experiment [1], and that vacancy-mediated climb dominates the evolution of dislocation network at higher temperatures.

2. The dynamics of climb and self-climb of dislocations

2.1. Vacancy-mediated climb

In a fully developed microstructure of an irradiated metal, vacancies are the only mobile point defects, the average concentration of which in the bulk of the material remains appreciable [10]. Thermal diffusion of vacancies drives the shrinkage and/or growth of dislocation loops. Dislocation climb, involving the bulk diffusion of vacancies (known as vacancy-mediated climb, VMC), is a well established mechanism of evolution of dislocation structures. The VMC velocity of a dislocation line segment is related to the vacancy concentration in the vicinity of a dislocation line $C(\mathbf{x})$ via a solution of the *stationary* diffusion equation $\nabla^2 C(\mathbf{x}) = 0$, which

neglects the effect of the elastic field of a dislocation, and the fact that the dislocation is in motion, on the diffusion of vacancies [30]. Noting the form of the Green function for the two-dimensional diffusion equation $G(\mathbf{x}) = \frac{1}{2\pi D} \ln(|\mathbf{x}|)$, we find an analytical expression for the concentration $C(\mathbf{x})$ of vacancies near a straight dislocation line [31]

$$C(\mathbf{x}) = C_{bulk} + \frac{C_{bulk} - C(\mathbf{x}_\Gamma)}{\ln\left(\frac{r_\infty}{r_c}\right)} \ln\left(\frac{|\mathbf{x}|}{r_\infty}\right), \quad (1)$$

where C_{bulk} is the concentration of vacancies at a large distance from the line Γ . $C(\mathbf{x}_\Gamma)$, or equivalently $C_\Gamma(\mathbf{x})$, is the concentration of vacancies in the immediate vicinity of line Γ at a distance r_c , which is the core radius of the dislocation. r_∞ is the outer cut-off radius, which is the distance from the dislocation Γ to a remote point in the microstructure. The VMC climb velocity is

$$v_{vmc} = \frac{2\pi r_c}{b_e} D_v (\nabla \cdot \mathbf{n}) C(\mathbf{x}) \Big|_{r_c}, \quad (2)$$

where D_v is the vacancy diffusion coefficient $D_v = D_0(T) \exp(-E_m/k_B T)$, $D_0(T)$ is a pre-exponential factor proportional to the product of the attempt frequency and the square of interatomic distance [32], E_m is the vacancy migration enthalpy, k_B is the Boltzmann constant, and T is the absolute temperature. \mathbf{n} is the unit vector in the climb direction $\mathbf{n} = \frac{\xi \times \mathbf{b}}{|\xi \times \mathbf{b}|}$, where ξ is the tangent unit vector to the dislocation line, and \mathbf{b} is the Burgers vector. Defining the edge component of the Burgers vector as $b_e = |\xi \times \mathbf{b}|$, from Eqs. (1) and (2) we find a convenient expression for the VMC velocity [31,33]

$$v_{vmc} = \frac{2\pi D_v}{b_e \ln\left(\frac{r_\infty}{r_c}\right)} (C_{bulk} - C_\Gamma), \quad (3)$$

where $C_\Gamma = C_0(T) \exp(-F^{cl} \Omega / b_e k_B T)$. Here, $C_0(T) = \exp(-E_f/k_B T)$ is the equilibrium concentration of vacancies per lattice site, E_f is the vacancy formation energy, and Ω is the atomic volume. F^{cl} is the climb force per unit length acting on the dislocation line.

Dislocation dynamics codes incorporate the vacancy diffusion-controlled dislocation climb into simulations through the climb velocity given by Eq. (3). This expression was derived assuming a straight line dislocation, and its form is *local* since it depends only on the Peach–Koehler (P-K) force acting on a selected dislocation segment. It does not apply to a general case of an arbitrary curved dislocation.

Gu et al. [34] generalised the treatment of climb using an integral form of the diffusion equation. In this approach, extended by Rovelli et al. [35,36] to include the treatment of free surfaces, the local VMC climb velocity is evaluated from an integral equation for the concentration of vacancies, defined at the dislocation lines and at internal and external surfaces of the material. The model, involving a quasi-stationary approximation, in which the field of vacancies is assumed to depend on time only through the time-dependence of the positions of dislocation lines and surfaces, treats the shape of the dislocation lines and their spatial configuration explicitly. The self-consistent quasi-stationary equation for the vacancy concentration, including dislocation climb, is [34–36]

$$\int_\Gamma \frac{b_e(\mathbf{x}') v_{cl}(\mathbf{x}')}{|\mathbf{x}_\Gamma - \mathbf{x}'|} dl(\mathbf{x}') = 4\pi D_v [C_{bulk} - C_\Gamma(\mathbf{x}_\Gamma)], \quad (4)$$

where $C_\Gamma(\mathbf{x}_\Gamma) = C_0(T) \exp\left(-\frac{F^{cl}(\mathbf{x}_\Gamma)\Omega}{b_e(\mathbf{x}_\Gamma)k_B T}\right)$ in thermal equilibrium, or $C_\Gamma(\mathbf{x}_\Gamma) = C_{bulk} \exp\left(-\frac{F^{cl}(\mathbf{x}_\Gamma)\Omega}{b_e(\mathbf{x}_\Gamma)k_B T}\right)$ in a general case, and $dl(\mathbf{x}')$ is a differential segment of dislocation line Γ .

In the limit where the concentration of vacancies far from the dislocation line is close its thermal equilibrium value $C_{bulk} = C_0(T)$,

Eq. (4) acquires the form

$$\int_{\Gamma} \frac{b_e(\mathbf{x}') v_{cl}(\mathbf{x}')}{|\mathbf{x}_{\Gamma} - \mathbf{x}'|} dl(\mathbf{x}') = 4\pi D_v [C_0(T) - C_{\Gamma}(\mathbf{x}_{\Gamma})], \quad (5)$$

If the parameters entering the expression for the self-diffusion coefficient of vacancies $D_{SD}^v(T) = D_0 \exp[-(E_f + E_m)/k_B T]$ [23,37] are determined from experimental observations, Eq. (5) can be written as

$$\int_{\Gamma} \frac{b_e(\mathbf{x}') v_{cl}(\mathbf{x}')}{|\mathbf{x}_{\Gamma} - \mathbf{x}'|} dl(\mathbf{x}') = 4\pi D_{SD}^v(T) \left[1 - e^{-\left(\frac{F^{cl}(\mathbf{x}_{\Gamma})\Omega}{b_e(\mathbf{x}_{\Gamma})k_B T}\right)} \right], \quad (6)$$

In applications, the self-diffusion coefficient $D_{SD}^v(T)$ can be deduced either from experimental observations or it can be estimated from the values of parameters E_f , E_m and D_0 computed using density functional theory. Below, we solve the integral Eqs. (4)–(6) for the dislocation climb velocities numerically, using a discretised representation of dislocation lines.

Before proceeding with the treatment, we note that the quasi-stationary approximation described above and adopted in our treatment, imposes limitations on the range of validity of the model. The model can be applied to the analysis of slow thermal evolution of microstructure driven by its own internal interactions but does not assume that the evolution of the dislocation network involves the action of a significant or time-dependent external load. Indeed, the presence of such load would imply the occurrence of fast movement of dislocations, the velocities of which are proportional to the respective, potentially high, Peach–Koehler forces. In this case, there is no guarantee that the field of vacancies would be able to follow the configuration of dislocations in the quasi-stationary sense, necessary to observe the validity of Eqs. (4)–(6).

In a material exposed to irradiation, the average volume concentration of defects can be as high as 0.1% [10,11] and is close to the concentration of vacancies at melting [22,23]. This is many orders of magnitude higher than the equilibrium concentration of vacancies in materials over the range of operating temperatures of fission or fusion reactors. Hence, the thermal equilibrium concentration of vacancies can often be neglected in comparison with the concentration of defects produced by irradiation. This also enables, where appropriate, using an approximate conservation law where, during annealing, the number of free vacancies lost from the medium equals the number of interstitial atoms eliminated from the dislocation loops.

The total number of interstitial defects N_{SIA} contained in self-interstitial dislocation loops can be evaluated from the ratio of relaxation volumes of the dislocation loops, computed in the elasticity theory limit [18,38], to the atomic volume Ω_0 , namely $N_{SIA} = \Omega_{rel}/\Omega_0$. The relaxation volume of a dislocation loop is [38]

$$\Omega_{rel} = \frac{1}{2} \oint \mathbf{b} \cdot (\mathbf{r} \times d\mathbf{l}), \quad (7)$$

where $d\mathbf{l}$ is a differential dislocation segment vector, $d\mathbf{l} = \boldsymbol{\xi} dl$, \mathbf{r} is the position vector of a dislocation segment, and \mathbf{b} is the Burgers vector of the loop. The sense of contour integration is chosen in such a way that the relaxation volume of an interstitial loop is positive, and the relaxation volume of a vacancy loop is negative.

In dislocation dynamics simulations, we use the boundary conditions that assume that the dislocation structures are immersed in an infinite homogeneous elastic medium. This model is reasonably accurate for the dislocation lines in the bulk of the material. The elastic stress generated by the loop segments is evaluated using the non-singular expressions derived by Cai et al. [39]. Calculations are performed in the adiabatic approximation [35,36] where vacancies are assumed to equilibrate on a timescale shorter than the timescale of evolution of dislocation loops. The numerical implementation of the force and climb in Discrete Dislocation Dynamics simulations is described in Appendix A.

2.2. Pipe diffusion-mediated dislocation self-climb

Models for the dislocation loops evolving by self-climb have until recently been restricted to the treatment of circular shapes, where the dynamics of each circular loop was controlled by a linear mobility law, describing its interaction with the local gradient of external stress [29,40]. Numerical parameters, describing pipe diffusion, were derived either from experimental observations or atomistic calculations [25,29,40,41].

Niu et al. [42] proposed a dislocation self-climb model suitable for the implementation in a discrete dislocation dynamics framework. In that model, self-climb conserves the volume of a dislocation loop as the loop changes its glide surface. It also describes the dynamics of volume-conserving interaction and the coalescence of loops and dislocations.

The self-climb velocity of a dislocation segment, forming a part of a pure prismatic loop, is [42,43]

$$v_{sc}(\mathbf{x}_{\Gamma}) = C_0 D_c b \frac{d^2}{ds^2} \exp\left(-\frac{F^{cl}(\mathbf{x}_{\Gamma})\Omega}{b k_B T}\right), \quad (8)$$

where D_c is the pipe-diffusion constant, s is the arc length, and $b = |\mathbf{b}|$ is the length of the Burgers vector of the loop.

Recently, the authors of Refs. [44,45] proposed another approach to the treatment of self-climb derived from a finite-element representation of diffusion in the dislocation core. Niu et al. [46] also developed a phase field model for the self-climb of prismatic dislocation loops.

The numerical implementation [43] of dislocation self-climb in a finite difference scheme gives the velocity of a node on a dislocation line \mathbf{P}_i in the form

$$v_{sc}(\mathbf{P}_i) = C_0 D_c b \frac{\frac{q(\mathbf{P}_{i+1}) - q(\mathbf{P}_i)}{L_{i,i+1}} - \frac{q(\mathbf{P}_i) - q(\mathbf{P}_{i-1})}{L_{i-1,i}}}{(L_{i-1,i} + L_{i,i+1})/2}, \quad (9)$$

where $q = \exp\left(-\frac{F^{cl}(\mathbf{P})\Omega}{b k_B T}\right)$ and $L_{i,i+1} = |\mathbf{P}_{i+1} - \mathbf{P}_i|$ is the length of a segment joining nodes \mathbf{P}_i and \mathbf{P}_{i+1} . This formulation maintains the relaxation volume of the loop as a conserved quantity as the loop evolves in a stress field [47]. In the approximation where a loop evolving by self-climb is assumed to maintain its shape [25,29,40,41,48], the loop undergoes a rigid translation in an external spatially varying stress field. The velocity of the translational motion equals [40,41]

$$v_{sc} = -\frac{2\nu \exp\left(-\frac{E_{sc}}{k_B T}\right) a^5}{\pi k_B T R^3} \frac{dE(x)}{dx}, \quad (10)$$

where R is the loop radius, $E(x)$ is the spatially varying energy of the loop interacting with an external stress field, ν is the attempt frequency, a is the lattice parameter and E_{sc} is the activation energy for self-climb.

Using Eq. (8) for the local self-climb velocity, Niu et al. [43] derived an analytical expression for the average translation velocity of a circular prismatic loop moving under the action of stress gradient

$$v_{sc} = -\frac{C_0 D_c \exp\left(\left(\frac{\sigma_{33}^0 + \sigma_{33}^{seif}}{k_B T}\right)\Omega\right) \Omega}{\pi k_B T R^3} \frac{dE(x)}{dx}, \quad (11)$$

The functional form of this equation agrees with Eq. (10). Comparing the coefficients in Eqs. (10) and (11), and neglecting the dependence of C_0 and $\exp\left(\left(\frac{\sigma_{33}^0 + \sigma_{33}^{seif}}{k_B T}\right)\Omega\right)$ on stress, we find that their product equals $4\nu a^2 \exp\left(-\frac{E_{sc}}{k_B T}\right)$. Hence, it becomes feasible to determine the self-climb velocity of a dislocation in a bcc ($\Omega = a^3/2$)

metal at a node \mathbf{P}_i as

$$v_{sc}(\mathbf{P}_i) = 4\nu a^2 \exp\left(-\frac{E_{sc}}{k_B T}\right) b \frac{\frac{q(\mathbf{P}_{i+1})-q(\mathbf{P}_i)}{L_{i,i+1}} - \frac{q(\mathbf{P}_i)-q(\mathbf{P}_{i-1})}{L_{i-1,i}}}{(L_{i-1,i} + L_{i,i+1})/2}, \quad (12)$$

Using extensive molecular statics calculations and kinetic Monte Carlo simulations, and exploring the energy landscape of pipe diffusion around irregular SIA prismatic loops in iron and tungsten, Swinburne et al. [40] showed that the rate-controlling activation energy parameter in Eqs. (8)–(12) for the $1/2\langle 111 \rangle$ or $\langle 100 \rangle$ loops equals 2 or 2.5 times the vacancy migration energy E_m . This procedure enables computing the self-climb velocity of a segment on a dislocation line using Eq. (12).

In a time-dependent simulation, the positions of nodes on a dislocation line are updated using the Euler forward method as

$$\mathbf{r}_i(t + \Delta t) = \mathbf{r}_i(t) + \mathbf{v}_i \Delta t, \quad (13)$$

where

$$\mathbf{v}_i = \mathbf{v}_{vmc} + \mathbf{v}_{sc}, \quad (14)$$

is the velocity of node i , and \mathbf{v}_{vmc} and \mathbf{v}_{sc} are given by Eqs. (4)–(6) and (12), respectively. The size of the time step Δt is determined by the maximum displacement rule applied to the highest velocity node.

3. Numerical simulations

3.1. Aluminium

To assess how well the predictions derived from the above model for the vacancy-mediated climb agree with the annealing times of dislocation loops observed experimentally, we simulate the thermal annealing of dislocation loops in face-centered cubic aluminium. Silcox and Whelan [28] observed the dynamics of annealing of prismatic vacancy dislocation loops in thin foils of quenched aluminium. A vacancy loop is formed when excess vacancies, produced by the rapid quenching of the material, condense into a disc-like cavity, which subsequently collapses into a loop bound by a dislocation line.

In a thin sample, surfaces act as sinks for vacancies emitted by the loops. The distance between a dislocation loop and the surface of a thin foil is of the order of $\sim 10^3$ Å, and hence a vacancy emitted by a loop reaches the surface before the next vacancy is emitted by the same loop. The vacancy supersaturation resulting from the emission of vacancies from dislocation loops is therefore very small, justifying the approximation where a loop is assumed to be embedded in a field of vacancies at thermal equilibrium. Hence, we can use Eq. (6) describing the interaction of dislocations with thermal equilibrium vacancies, to evaluate the rate of shrinkage of vacancy loops.

When selecting the vacancy diffusion parameters in the climb model (6), because of the exponential sensitivity of numerical results to the choice of migration and formation energies [36], there is a notable difference between the self-diffusion rates predicted from the tracer diffusion data [49] and the nuclear magnetic resonance (NMR) data [50]. Calculations by Sandberg et al. [51] of the vacancy diffusion rates agree better with the tracer diffusion data [49]. To assess the effect of variation of parameters on the predicted dislocation evolution timescales, we have simulated the evolution of a vacancy dislocation loop using both the tracer and NMR vacancy diffusion data.

In the experiment [28], an isolated vacancy loop situated ~ 1000 Å away from the surface was observed shrinking under its self-stress at $T = 470$ K. Fig. 1 shows the comparison of annealing curves observed in experiments [28] and those derived from a simulation of a vacancy loop evaporation as a function of time. The error bars indicate the experimental uncertainty in the position of

dislocation lines [28]. Since the self-diffusion coefficient was not directly measured at 470 K, we have extrapolated its value from calculations [51] and experiment [50]. The resulting self-diffusion coefficients are $D^r = 6.082$ Å²/s and $D^{NMR} = 42.34$ Å²/s. The Arrhenius extrapolation is justified here since the self-diffusion coefficient follows the Arrhenius law in the temperature range from 500 to 800 K. Note that the experimentally observed vacancy formation and migration energies in Aluminium are 0.68 eV and 0.61 eV, respectively [51].

The effective shear modulus ($\mu = 23.498$ GPa) and the Poisson ratio ($\nu = 0.353$) of Aluminium were derived from the experimentally measured elastic constants [52] using a homogenization scheme [53]. The lattice parameter, and the corresponding atomic volume, as well as the Burgers vector at $T = 470$ K, were obtained from Ref. [54]. The results illustrated in Fig. 1 and obtained from Eq. (6) appear quantitatively different but are in fact qualitatively similar. We note that better agreement with experiment is achieved if the tracer self-diffusion data [51] are used as input parameters.

Given the good agreement between the observed and simulated vacancy loop annealing curves, and noting that the average distance between the loop and the surface is ~ 1000 Å, as found in experiment, it appears that the surface effect is not strong enough to significantly affect the loop annihilation rate.

The form of the curves shown in Fig. 1 is similar, and this enables a quantitative analysis of the annealing process. The rate of shrinkage of the loop exhibits distinct features. As a function of time, the process is not uniform, and it strongly depends on the size of the loop. As the loop gets smaller, the rate of its shrinkage accelerates and becomes extreme in the limit $r \rightarrow 0$, in agreement with experiment [28]. It proved not possible to follow the evolution of very small loops because their rate of shrinkage was too high. The very steep slope of the radius versus time curve in the small radius limit was verified using the ciné-techniques, although establishing an accurate functional form of the curve in that limit was not possible. Observations agree well with the simulations based on the tracer vacancy diffusion data, with the slope of the curve changing from 9 Å/s at $r = 100$ Å to 84 Å/s at $r = 50$ Å.

3.2. Tungsten (W)

Body-centered cubic tungsten is a candidate material for the plasma-facing components of fusion plasma devices, including the ITER divertor [55]. Un-irradiated tungsten exhibits relatively low hydrogen isotope retention, it has a high melting point, low erosion rate, and good thermal conductivity [56]. Pure crystalline or industrially produced tungsten is brittle at room temperature, and the brittle-to-ductile transition temperature (BDTT) of pure crystalline tungsten is relatively high ~ 673 – 773 K [57]. The BDTT temperature increases further due to the accumulation of defects produced by irradiation. These defects are the dislocation loops, voids, and transmutation products, and their accumulation result in the general deterioration of thermo-mechanical properties [58–60].

There are five stages of recovery of electrical resistivity that are commonly identified in tungsten irradiated by fast neutrons. Stages III, IV and V are within the interval of expected operating temperatures of a fusion reactor from 773 K to 1273 K [61]. Stage III of resistivity recovery, with the onset temperature of ~ 550 K, is related to the onset of thermal diffusion of mono-vacancies [62–64]. Stage IV is observed close to ~ 811 K, and is believed to be associated with the dissociation of vacancy-impurity complexes [65–68]. The origin of stage IV recovery¹ was a subject of debate [66,69] that has now been resolved by density functional theory (DFT) calcula-

¹ Ref. [65] refers to this stage as an intermediate recovery temperature region.

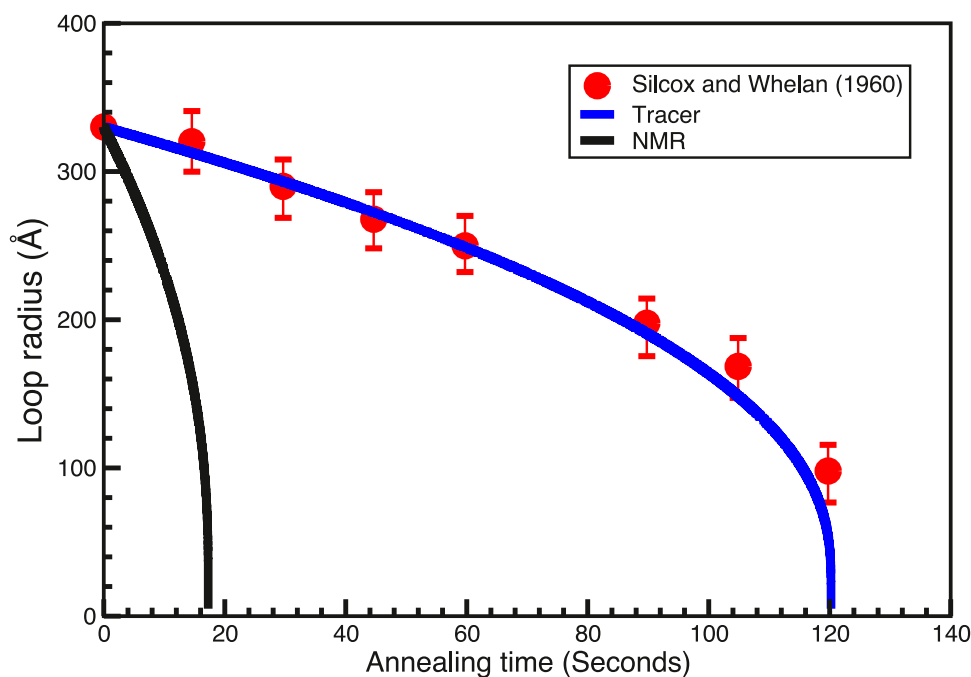


Fig. 1. Radius of a vacancy loop in aluminium plotted as a function of the annealing time. Simulations were performed assuming $T = 470$ K. The curves were computed using the activation energy parameters derived from the macroscopic-tracer (Tracer) experiments [51] and from the microscopic-nuclear-magnetic-resonance (NMR) self-diffusion data [50].

tions. DFT calculations show that stable di-vacancies do not form in tungsten [70,71]. The effective activation energy corresponding to stage IV, obtained from the resistivity recovery measurements, is close to 3.3 eV [65]. DFT calculations predict that the dissolution energy of carbon-vacancy complexes is in the range from 3 eV to 3.43 eV [68]. This is broadly similar to the activation energy found in experiment [65], suggesting that stage IV of resistivity recovery [65], corresponding to temperatures in the range from ~ 811 K to 1143 K, is likely related to the dissociation and dissolution of vacancy-carbon complexes. The temperature of stage V is close to 1143 K [67], and its nature is not entirely clear, although this stage appears to be associated with the evaporation of defect clusters and the formation and evolution of voids [67].

Several experimental studies [1,58,72] explored the effects of radiation damage and dynamics of dislocations in tungsten. These studies classified defects formed in collision cascades, and explored the recovery of microstructure as a function of annealing temperature and time. There are notable differences between the temperatures quoted in literature at which dislocation loops evolve and exhibit effects of thermal annealing. For example, Ferroni et al. [1] found that dislocation loops vanish after 1 h at 1400 °C (1673 K), whereas Hu et al. [58] observed a complete recovery of dislocation microstructure after 1 h annealing at a lower temperature of 1000 °C (1273 K).

The microstructures studied by Ferroni et al. [1] were produced by 2 MeV W^+ ion irradiation exposure to a relatively high dose of 1.5 dpa at $T = 500$ °C, which is above the temperature of stage III resistivity recovery in pure crystalline tungsten. The use of ion irradiation for simulating effects of fusion neutron irradiation has some limitations since ion irradiation produces a different spectrum of primary knock-off atoms (PKAs), in addition to the effects of associated with the presence of the substrate [10] and the proximity of the surface [36].

The experimental study by Hu et al. [58] explored single crystalline tungsten exposed to fission neutron irradiation at 90 °C to the lower dose of 0.03 dpa. The defect microstructure produced by irradiation was characterised using transmission electron mi-

croscopy following 1 h annealing at 500 °C, 800 °C, 1000 °C and 1300 °C. The study does not provide data on the annealing rates but still offers a qualitative view of the effect of annealing on the population of loops. Electron microscope images show a marked reduction of the dislocation loop density after one hour annealing at 800 °C, and the complete absence of loops after one hour annealing at 1000 °C. The study also noted that the loss of interstitial loops occurring in the temperature range 500–800 °C was correlated with the positron annihilation spectroscopy data, indicating the reduction of the density of intermediate-size vacancy clusters, and growth of large vacancy clusters, likely through the Ostwald ripening process involving the emission of monovacancies by smaller vacancy clusters and capture of vacancies by the larger clusters.

Electron microscope characterization of dislocation loops produced in tungsten by self-ion irradiation [1] showed that the loops predominantly were of the $1/2\langle 111 \rangle$ type and were mostly interstitial in nature. The dominance of the $1/2\langle 111 \rangle$ loops correlates with the results of high-temperature neutron irradiation [73], and agrees with the notion that the $\langle 100 \rangle$ -type loops form in high-energy cascades and subsequently get absorbed by the larger $1/2\langle 111 \rangle$ loops through dislocation reactions [74,75].

3.2.1. Low doses, lower temperature irradiation

To model the thermal evolution of the dislocation loop microstructure formed at a relatively low dose and lower irradiation temperature, we need to ensure that the microstructure modelled in simulations is comparable with the microstructure formed in experiment. For example, it is desirable to use the appropriate size distribution of the loops. Indeed, the loop size affects their annealing rates and annihilation times. In simulations, we created a dislocation loop microstructure consisting of $1/2\langle 111 \rangle$ -type Burgers vector, as observed in experiment [58] (0.03 dpa and 90 °C), and used the observed loop size distribution. The loop radii varied in the interval between 10 and 25 Å, and the volume density of loops was close to 3.05×10^{22} loops/m³. One hundred dislocation loops were distributed homogeneously in a cubic simulation cell with linear

dimensions of 1486 Å. This dislocation loop microstructure corresponds to the volume-average self-interstitial atom content C_{int} of 5.83×10^{-5} per lattice site. Simulations in this Section 3.2.1 were performed using Eq. (4), describing the interaction of the dislocation loop microstructure with supersaturated vacancies.

The values of the shear modulus, the Poisson ratio and the lattice parameter used in the simulations were 161 GPa, 0.28 and 3.1795 Å [76], respectively. The Burgers vector of the $1/2(111)$ loops is 2.753 Å.

We consider the case of high purity tungsten where the impurity content is so low that the individual vacancies are not bound to any foreign interstitial atoms. Monovacancies are assumed to migrate freely, and interaction between the vacancies is not taken into account. Positron annihilation spectroscopy experiments [64], in agreement with the earlier data by Thompson [62] and Rasch et al. [77], show that the diffusion of monovacancies is activated at ~ 550 K, corresponding to the vacancy migration barrier of $E_m = 1.85$ eV.

Vacancy migration energies derived from DFT calculations for tungsten vary in a relatively narrow range [20]. We note that DFT calculations, apart from Ref. [78], do not aim at determining the diffusion coefficient, and only evaluate the energy barriers for the migration of defects. In Ref. [78], the monovacancy migration energy was found to be close to $E_m = 1.93$ eV and the pre-exponential factor was determined to be $D_0 = 7 \times 10^{13}$ Å²/s. Mundy and collaborators [79] investigated self-diffusion in tungsten and experimentally measured the self-diffusion coefficient D_{SD}^v over the temperature range from 1700 K to 3400 K. The $D_{SD}^v(T) = 4 \times 10^{14} \exp(-\frac{5.45 \text{ eV}}{k_B T})$ Å²/s term was found to dominate the tracer diffusion curve at temperatures below 2400 K and was identified as corresponding to self-diffusion mediated by monovacancies [77,79]. In agreement with Mundy et al. [79], Rasch et al. [77] found $E_m = 1.78$ eV and $E_f = 3.67$ eV. The use of the above vacancy parameters over the range of temperatures explored here is justified since the activation enthalpy of a monovacancy can be taken as temperature-independent below $0.66T_m$, where only the single vacancy diffusion mechanism plays a part [64,77,79].

At the the start of each simulation, C_{bulk} was set to $C_V + C_0(T)$ where $C_V = C_{int} = 5.83 \times 10^{-5}$ per lattice site. C_{bulk} decreases as a function of annealing time as vacancies are absorbed by the interstitial loops. At the end of each simulation, when all the loops vanish, the concentration of vacancies decreases to its thermal equilibrium value $C_0(T)$. Fig. 2(a,b) show the variation of the total length and the total relaxation volume of dislocation loops after 1 h isochronal annealing. The microstructure shows sensitivity to temperature starting from 650 K where the loop volume loss is 3.34% if the parameters used in the simulations are taken from experimental observations [77,79]. Simulations describing the evolution of loops at 750 K exhibit 4% volume loss if the input parameters are taken from DFT calculations [78].

Simulations show that approximately 2200 s are required to completely anneal the dislocation microstructure at 873 K if the vacancy parameters are taken from experimental observations. The ~ 100 K shift of the curve marked by triangles in Fig. 2 stems from the use of DFT data from Ref. [78], where the diffusion barrier for monovacancies is slightly overestimated (1.93 eV) and where the pre-exponential factor ($D_0 = 7 \times 10^{13}$ Å²/s) is 5.71 smaller than the value found in experiment (namely, $D_0 = 4 \times 10^{14}$ Å²/s) [79]. The comparison of curves in Fig. 2(a,b) illustrates the effect of variation of parameters D_0 and E_m on the microstructural evolution. The predicted onset temperature of 650 K for the loop loss, derived from the experimental input data, is relatively close to the monovacancy migration onset temperature ~ 550 K [64] found using tungsten irradiated with 10-MeV H⁺ ions at 35 K. This places

the annihilation of interstitial loops, formed in pure tungsten at low irradiation dose and very low temperature, firmly within the stage III resistivity recovery temperature range.

The difference between the recovery onset temperature (650 K) found in simulations and that found in experiment [64] (550 K) can be attributed to the fact that the interval spanned by the loop radii 10–25 Å, derived from Ref. [58], is relatively large. Also, the initial bulk vacancy concentration $C_V = C_{int} = 5.83 \times 10^{-5}$ per lattice site is relatively low.

New positron annihilation spectroscopy (PAS) measurements [80] show that the vacancy defects, formed following room temperature irradiation of tungsten by 2 MeV W⁺ ions to low dose of 0.0085 dpa, were predominantly monovacancies. The PAS measurements find that the concentration of monovacancies is close to 10^{-3} per lattice site. Fig. 3(a,b) compare the effects of thermal evolution of dislocation microstructure for C_{bulk} taken in the form $C_{int} + C_0(T)$ or $C_{bulk} = 10^{-3}$. The dislocation loop microstructure appears sensitive to 1 h annealing already at 590 K, if the $\sim 2.6\%$ volume loss is taken as a criterion, provided that the starting vacancy concentration of $C_{bulk} = 10^{-3}$ is used. This brings our predictions in agreement with observations described in Ref. [64]. We also note that an independent study of ion irradiated tungsten [81] also concluded that in the limit of high irradiation dose the average bulk vacancy concentration was 3×10^{-3} , which is close to the value used in the simulations described here.

Sensitivity of the annealing curves to the vacancy parameter used
We now try to rationalize the difference found in the simulations of microstructural annealing performed using two different vacancy and diffusion parameter sets in Fig. 2(a,b). The characteristic timescale τ of thermally activated microstructural evolution follows the Arrhenius law [82]

$$\tau^{-1} \sim \nu \exp\left(-\frac{U}{k_B T}\right), \quad (15)$$

where U is the activation energy for the dominant low-barrier mode of evolution and ν is the attempt frequency to cross the low-barrier U . Vacancies are the only thermally mobile point defects in irradiated tungsten in the temperature interval studied here, and hence in the above Arrhenius equation U is the vacancy migration energy E_m and ν is the frequency of oscillations of an atom at a lattice site in tungsten ($\nu \sim 10^{14} - 10^{15}$ s⁻¹). The temperature at which the microstructure evolves into a certain reduced damage state D_α after thermal annealing over a certain interval of time τ_α can be derived from Eq. (15) as

$$T_\alpha \sim \frac{1}{\left[\ln(\tau_\alpha \cdot \nu)\right]} \frac{E_m}{k_B}, \quad (16)$$

As we compare microstructural recovery over a specific time interval τ_α for two different vacancy migration energies, similar level of recovery D_α can be achieved at two different annealing temperatures. The absolute difference between the two annealing temperatures is

$$\Delta T_\alpha \sim \frac{1}{\left[\ln(\tau_\alpha \cdot \nu)\right]} \frac{|\Delta E_m|}{k_B}, \quad (17)$$

The total relaxation-volume loss curves in Fig. 2 were determined using the vacancy migration energy barriers derived from experiment 1.78 eV [77,79] and from *ab initio* calculations 1.93 eV [78], hence corresponding to $\Delta E_m = 0.15$ eV. The Arrhenius estimate for the absolute difference between the two temperatures ΔT_α , resulting in similar damage recovery after $\tau_\alpha = 1$ h, can be evaluated from Eq. (17) to be ~ 43 K.

Other than the vacancy migration energies (1.78 eV versus 1.93 eV), the two-parameter set used in the simulations shown in Fig. 2 also differ by the pre-exponential diffusion factors D_0 (4×10^{14} versus 7×10^{13} Å²/s). To draw a valid comparison with

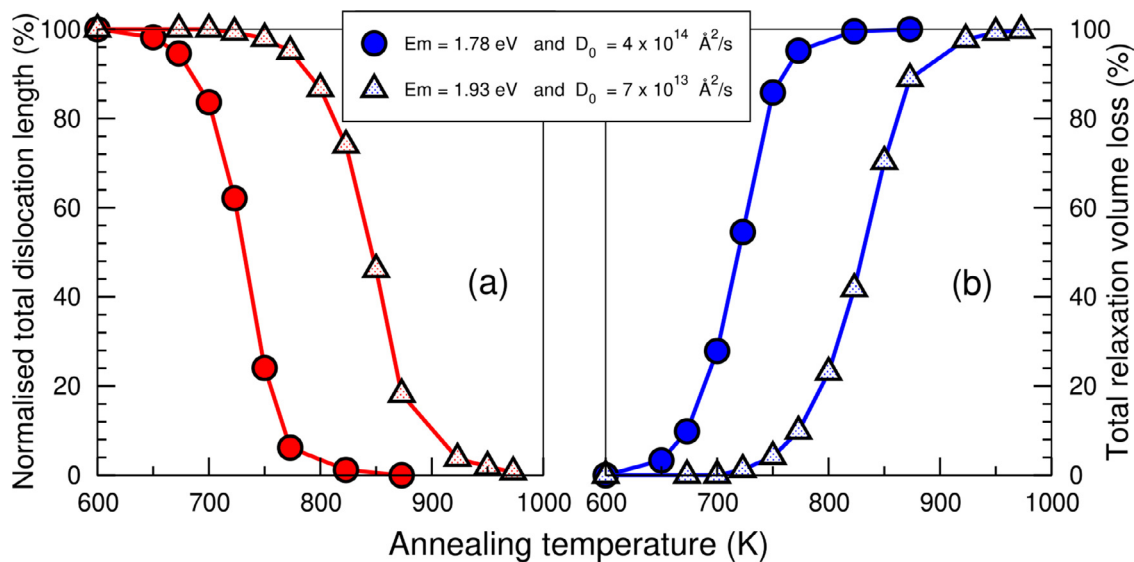


Fig. 2. Curves illustrating the evolution of the dislocation loop microstructure in tungsten at a constant temperature. The microstructure is characterized by (a) the total length of the dislocation lines and (b) the loss of the relaxation volume of dislocation loops, in percent, after 1 h isochronal annealing. The data shown by solid circles and triangles were obtained using the input parameters derived from experiment [77,79] and from DFT calculations [78], respectively.

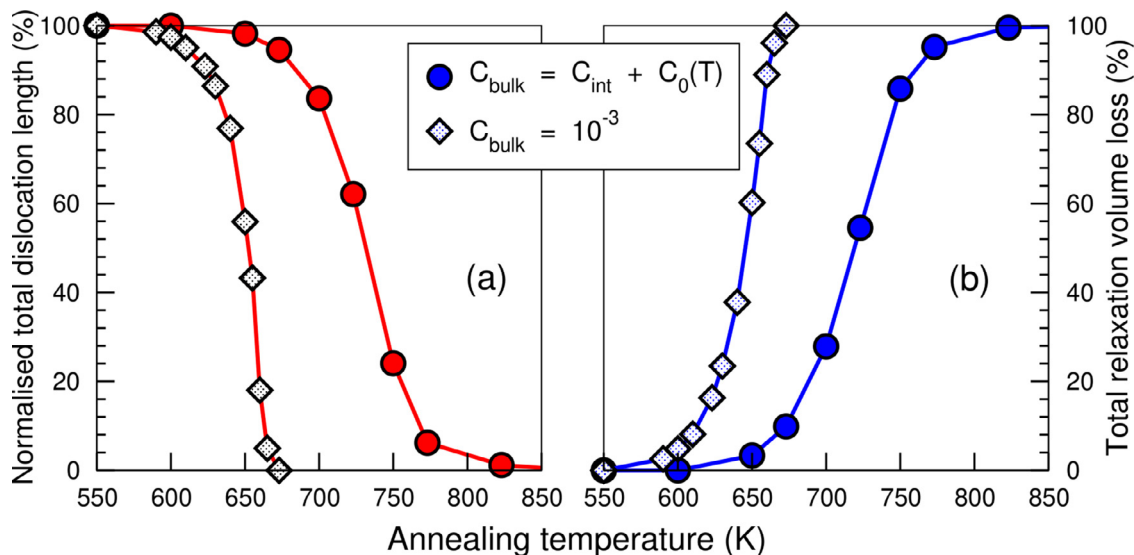


Fig. 3. Curves illustrating the evolution of the dislocation loop microstructure in tungsten at a constant temperature. Dislocation microstructure is characterized by (a) the total length of the dislocations and (b) the loss of relaxation volume of dislocation loops, in percent, after 1 h isochronal annealing. Both data sets (solid circles and diamonds) were produced using input parameters derived from experiment [77,79]. Simulations differ from those illustrated in Fig. 2 by the choice of bulk vacancy concentration C_{bulk} .

Table 1

Various damage recovery levels and the corresponding absolute temperature difference ΔT evaluated from the annealing curves simulated assuming $D_0 = 4 \times 10^{14} \text{ \AA}^2/\text{s}$ and shown in Fig. 4.

Damage recovery (%)	3.34	9.86	27.87	54.54	85.81	95.20
ΔT (K)	50	51	53	57	60	62

the Arrhenius estimate for the absolute temperature difference ($\Delta T_{\alpha} \sim 43 \text{ K}$), we performed new simulations for $E_m = 1.93 \text{ eV}$ and $D_0 = 4 \times 10^{14} \text{ \AA}^2/\text{s}$. The results of new simulations together with other annealing curves are shown in Fig. 4.

The total relaxation volume loss and damage recovery levels extracted from the two annealing curves, simulated assuming $D_0 = 4 \times 10^{14} \text{ \AA}^2/\text{s}$ and shown in Fig. 4, are given in Table 1, together with the corresponding ΔT 's. The average absolute temperature difference ΔT_{ave} derived from a set of ΔT values shown in

Table 1 is $\sim 55 \text{ K}$, in agreement with the Arrhenius estimate of $\Delta T_{\alpha} \sim 43 \text{ K}$, derived from Eq. (17). This shows that the computational model based on discrete dislocation dynamics simulations can indeed describe reasonably accurately the thermal evolution of a dislocation loop microstructure.

Number density, relaxation volumes and annihilation of the dislocation loop microstructure

We now analyze the number density and the total relaxation volume of dislocation loops as functions of temperature and time. The results correspond to the simulations performed using the diffusion input parameters derived from experiment [77,79], namely $D_0 = 4 \times 10^{14} \text{ \AA}^2/\text{s}$, $E_m = 1.78 \text{ eV}$, and the initial condition $C_{bulk} = C_{int} + C_0(T)$.

Despite the fact that the population of loops start evolving already at 650 K, the volume density of loops remains almost constant up to 723 K, as illustrated in Fig. 5. The figure also shows that approximately half of all the loops vanish after 1 h annealing

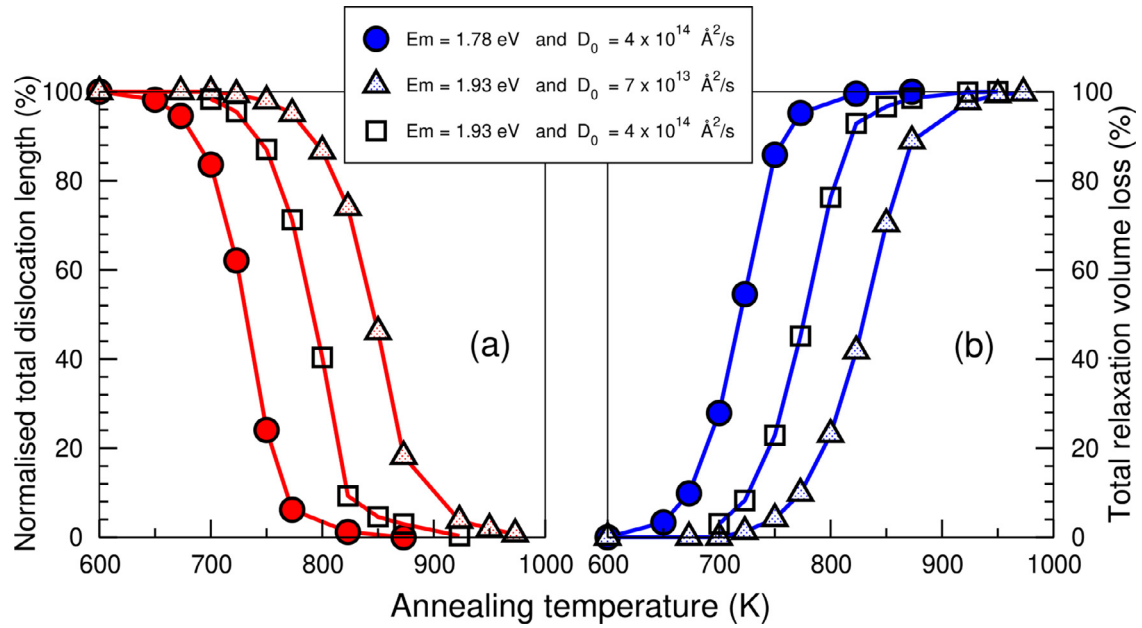


Fig. 4. Curves illustrating the evolution of the dislocation loop microstructure in tungsten at a constant temperature. The microstructure is characterized by (a) the total length of dislocation lines and (b) the loss of relaxation volume of dislocation loops, in percent, after 1 h isochronal annealing. The data shown by solid circles and triangles were obtained using the input parameters derived from experiment [77,79] and from *ab initio* calculations [78], respectively. The data shown by squares were obtained using an adjusted vacancy parameter set used for comparison, as explained in the text.

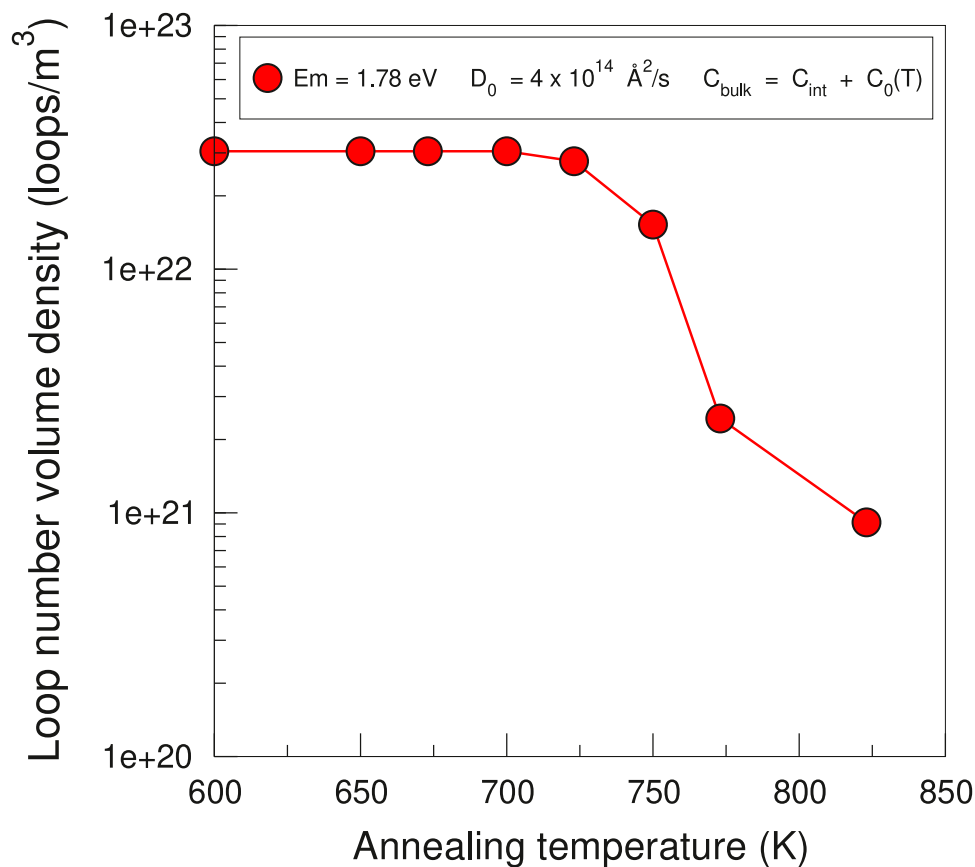


Fig. 5. Variation of the number density of dislocation loops as a function of temperature after one hour isochronal annealing in tungsten. The data were obtained using the input parameters derived from experiment [77,79], assuming the initial vacancy concentration $C_{bulk} = C_{int} + C_0(T)$.

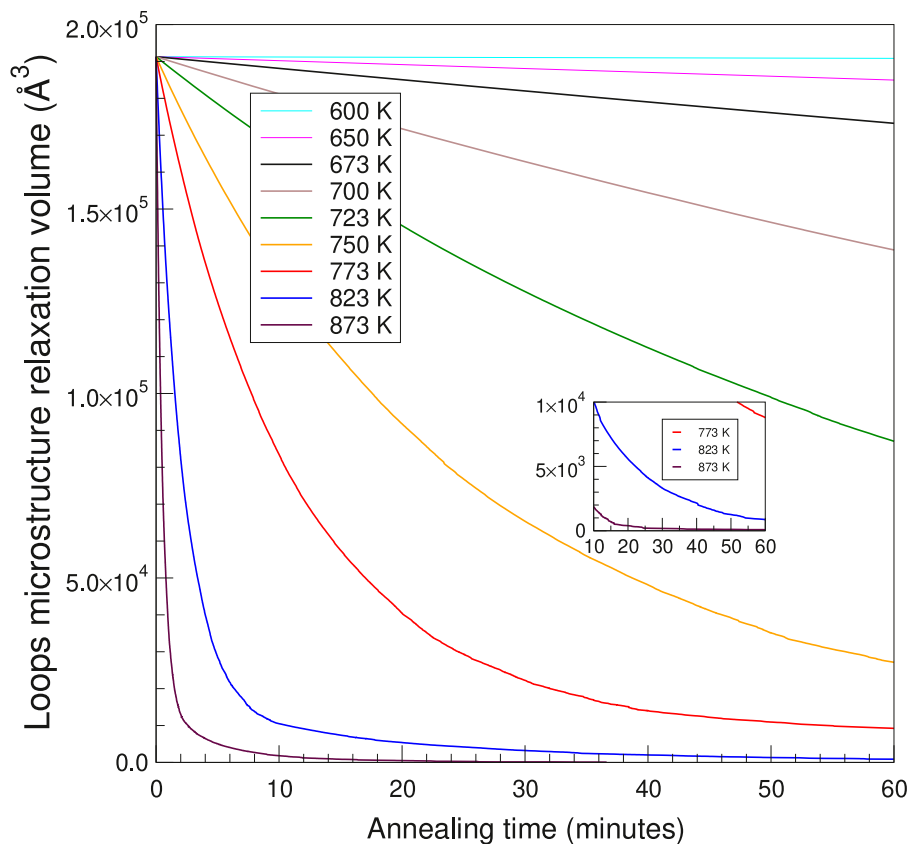


Fig. 6. Annealing curves showing the variation of the total relaxation volume of dislocation loop microstructure simulated for several temperatures in tungsten. The data were obtained using the input parameters derived from experiment [77,79], specifically, the pre-exponential factor $D_0 = 4 \times 10^{14} \text{ \AA}^2/\text{s}$, vacancy migration energy $E_m = 1.78 \text{ eV}$ and the initial vacancy concentration $C_{\text{bulk}} = C_{\text{int}} + C_0(T)$.

at 750 K, and very few loops remain after annealing above 823 K. The smallest loops are eliminated first, and this is consistent with that the elastic climb forces driving the evolution are the largest for the small loops.

The curves, showing how the total relaxation volume of dislocation loops varies with time, exhibit a common feature illustrated in Fig. 6. Namely, the total relaxation volume varies non-linearly at a rate that increases with temperature. This is particularly notable at higher temperatures, where the curves exhibit two intervals of annealing. The first interval, if we take the 823 K curve as an example, is characterised by a very steep descent in the first 10 min, followed by a longer interval where the curve appears to be levelling off. As shown in the inset, the 823 K curve still goes downwards over the second time interval, albeit at a slower rate than during the initial short rapid annealing interval. The reason for the variation of the slope of the curve is the varying vacancy concentration. At the start of annealing, the concentration of monovacancies in the bulk is $\sim 5.83 \times 10^{-5}$ per lattice site. The majority of monovacancies react with dislocation loops over the first 10 min of annealing at 823 K, eliminating the smallest loops with radii from 10 and 15 Å, and a significant fraction of larger loops with radii from 20 and 25 Å. By this time the concentration of excess monovacancies decreases to $\sim 0.32 \times 10^{-5}$, which amounts to around 94% reduction in comparison with the initial concentration of monovacancies.

The effective activation energies characterising the dynamics of annealing of dislocation loop microstructure can be extracted from the gradient of linear fits to the Arrhenius plots shown in Fig. 7. This yields the activation energies in the range from $\sim 1.78 \text{ eV}$ to $\sim 1.90 \text{ eV}$ that are close to the monovacancy migration energies of

1.78 eV or 1.93 eV used in the simulations. These activation energies do not correspond to the monovacancy self-diffusion energy $E_f + E_m$, because the monovacancies responsible for the annihilation of dislocation loops are generated by irradiation, and the dynamics of annealing process does not involve the thermal formation of vacancies at surfaces.

Loop annihilation: simulations versus experiment, and the role of impurities We now attempt to explain the difference between the loop annihilation temperatures found in simulations and in experiment [58]. On the one hand, we find that the evolution of loops is sensitive to the migration of monovacancies, with annealing starting at 650 K (1 h annealing time), leading to their complete elimination at 873 K. On the other hand, Hu et al. [58] observed that the full elimination of loops by annealing required reaching the temperature of 1000 °C (1273 K). Transmission electron microscope (TEM) images show the coarsening of loops after 1 h at 500 (773 K) and 800 °C (1073 K), where the number of large loops after 800 °C annealing was higher than after annealing at 500 °C. The latter can be explained by reactions between the gliding loops and by loops absorbing the mobile self-interstitial defects and small self-interstitial defect clusters.

Chemical analysis of the samples showed non-negligible impurity content, including the presence of 20 ppm carbon. Carbon impurities trap monovacancies, impeding their diffusion. For example, a monovacancy can trap up to four carbon atoms to form C_nV ($n=1,2,3,4$) complexes, where C_1V , C_2V and C_3V represent the most stable configurations with binding energies of 1.93, 1.97 and 1.87 eV, respectively. These values are higher than the binding energy of the C_4V configuration that, according to DFT calculations, equals 1.54 eV [83]. Hence, a significant number of monovacancies

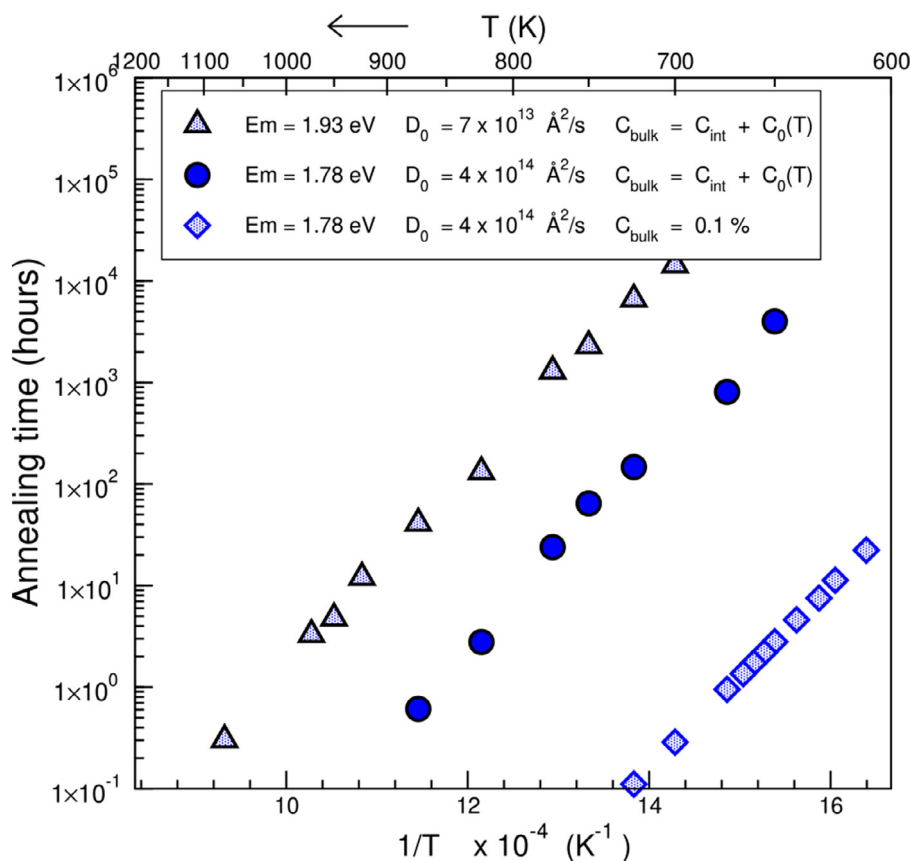


Fig. 7. Arrhenius plots of annihilation times characterising the thermal evolution of interstitial dislocation loops in tungsten. The legend referring to each data set describes the input parameters used and the choice of the initial bulk vacancy concentration C_{bulk} .

is expected to be trapped by carbon and other impurities below 1000 °C.

The size distribution of three-dimensional vacancy clusters derived from positron annihilation spectroscopy (PAS) [58], shows an increase of large vacancy cluster concentration after annealing in the temperature interval between 400 °C (673 K) and 800 °C (1073 K). This can occur by the absorption of monovacancies, suggesting that free mobile monovacancies still exist in this temperature range. However, mobile monovacancies do not annihilate loops at 500 and 800 °C, indicating that the number of freely migrating monovacancies below 1000 °C is not high. In fact, the total concentration of various 3D vacancy clusters in the as-irradiated state is about $2.8 \times 10^{24} \text{ m}^{-3}$ [58]. This is almost two order of magnitude higher than the loop number density ($3.05 \times 10^{22} \text{ m}^{-3}$). The vacancy clusters, in addition to the interstitial loops, act as sinks for mobile monovacancies. The high density of vacancy clusters compared to the interstitial loops reduces the number of the available free monovacancies able to diffuse to the loops and annihilate them.

The fact that the experimental observations by Hu et al. [58] show the full annealing of loops only after 1 h at 1000 °C (1273 K) could be explained by the dissociation of vacancy-impurity complexes that produces a sufficient amount of free monovacancies capable of annihilating the loops. This also explains the difference between the predicted and observed temperatures at which full annihilation of loop occurs.

To further explore the evolution of loops at 1273 K interacting with thermal equilibrium vacancies, we simulated the evolution of an interstitial loop of radius $r = 10 \text{ \AA}$ using Eq. (5). The loop's radius corresponds to the smallest size of the loops noted in Ref.

[58]. The vacancy parameters used in the simulations were derived from experimental observations [77,79], and are $D_0 = 4 \times 10^{14} \text{ \AA}^2/\text{s}$, $E_m = 1.78 \text{ eV}$ and $E_f = 3.67 \text{ eV}$. We found that the loop remained stable over a period of a few hours, further confirming that the thermal evolution of dislocation loops observed in Ref. [58] could only be explained by their interaction with the excess concentration of monovacancies generated by irradiation.

3.2.2. High irradiation dose and temperature

If a bulk tungsten sample is irradiated at a temperature above that of stage III, corresponding to the onset of vacancy migration, there is no reason to expect that excess vacancies would accumulate in a material during irradiation.

The process of annealing of interstitial loops in this case occurs by the absorption of thermal vacancies, the concentration of which at ambient or slightly elevated temperature is very small [22,23]. In thermal equilibrium conditions, if an interstitial loop climbs by absorbing a thermal vacancy, the material recovers this vacancy from a void in the bulk of the material or from the outer surface of the sample. This mode of thermal annealing was observed in experiments on EUROFER97 steels irradiated with neutrons to 15 dpa [84], where the rate of annealing was found to be controlled by the thermal equilibrium vacancies. Dislocation tangles were considered as possible vacancy sources [84], although no specific attribution of the vacancy sources is required for the interpretation of annealing experiments performed under thermal equilibrium conditions.

Annealed bulk tungsten samples still showed the presence of interstitial loops after one hour annealing at 1073 K, 1223 K and 1373 K, see Ref. [1]. The number density of loops and their size distribution changed significantly as a function of the annealing

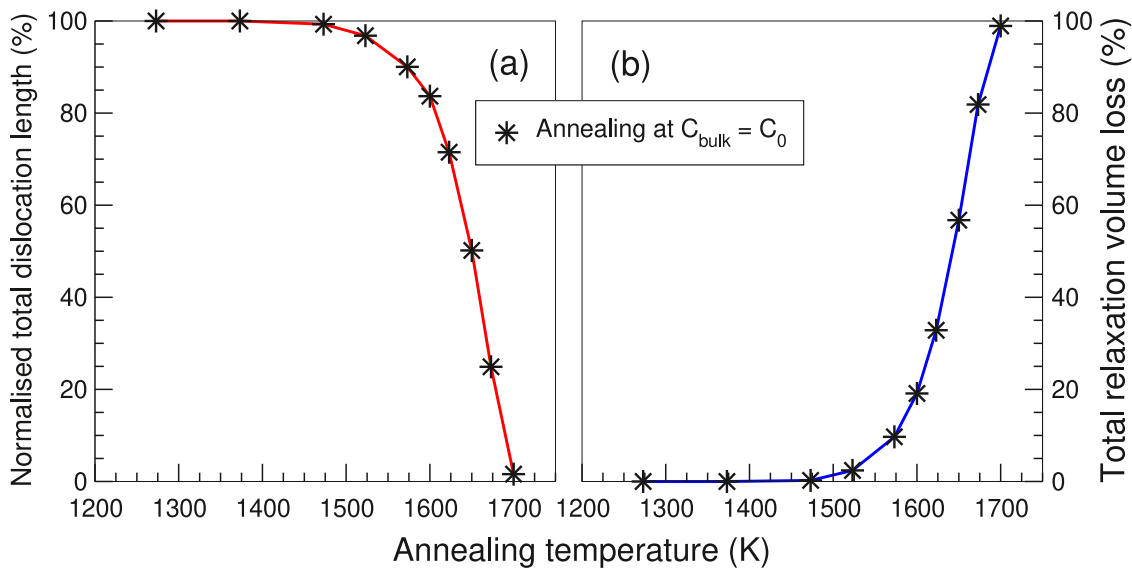


Fig. 8. Evolution of interstitial dislocation loop microstructure *via* VMC. (a) the total length of dislocation lines and (b) the corresponding microstructure volume loss, in percent, after 1 h isochronal annealing of tungsten. The data were obtained using the input parameters derived from experiment [77,79] ($D_0 = 4 \times 10^{14} \text{ \AA}^2/\text{s}$, $E_m = 1.78 \text{ eV}$, $E_f = 3.67 \text{ eV}$), and the initial thermal equilibrium concentration of vacancies $C_{\text{bulk}} = C_0(T)$.

temperature. The loops did not vanish until the annealing temperature reached 1673 K. The fact that such a high temperature was required to eliminate the loops indicates that annealing of loops involved primarily the absorption of equilibrium thermally-generated vacancies.

This scenario is corroborated by the analysis of thermal evolution of voids. The voids were observed already at 1073 K, at a high density approaching $6 \times 10^{26} \text{ voids/m}^3$, providing evidence that vacancy clusters initially scattered in the matrix did condense into mesoscopic voids. The average diameter of voids ($\sim 15 \text{ \AA}$) and their number density remained constant up to 1373 K. While Ref. [1] provides no experimental data on loop annealing in the temperature interval from 1373 K to 1673 K, observations at 1673 K show a reduction of the void number density and increase of the average size of the voids. Experimental observations indicate that the voids size and density are related to the interstitial loops disappearance observed at 1673 K.

We simulate a dislocation microstructure corresponding to high dose (1.5 dpa) and high temperature irradiation (773 K) experiment [1] by considering an ensemble of interstitial loops with the $1/2\langle 111 \rangle$ -type Burgers vectors, evolving *via* vacancy-mediated climb. The dislocation microstructure is taken as the as-irradiated loops size distribution, with the volume density of loops being equal to that found in experiment [1]. We distributed one hundred loops in a cubic simulation cell with linear dimensions of 3218 \AA . The volume density of loops is $3 \times 10^{21} \text{ loops/m}^3$, whereas the loop radii vary from several \AA to approximately 55 \AA . Similarly to Section 3.2.1, the values of the shear modulus, the Poisson ratio and the lattice parameter used in the simulations were 161 GPa, 0.28 and 3.1795 \AA [76], respectively. The Burgers vector of the $1/2\langle 111 \rangle$ loops is 2.753 \AA . Simulations were based on Eq. (5) describing the interaction of the dislocation loop microstructure with thermal vacancies. The vacancy parameters were derived from experiment [77,79], namely, $D_0 = 4 \times 10^{14} \text{ \AA}^2/\text{s}$, $E_m = 1.78 \text{ eV}$, and $E_f = 3.67 \text{ eV}$. Fig. 8(a,b) present the variation of the normalised total dislocation length of dislocation lines and the total relaxation volume loss, in percent, as a function of the annealing temperature, after 1 h isochronal annealing. As shown in Fig. 8(a,b), the dislocation loop microstructure is insensitive to 1 h anneal at intermediate temperatures. The normalised total length of disloca-

tion lines and the microstructure relaxation volume become sensitive to 1 h anneal at 1523 K i.e. the number of thermal equilibrium vacancies diffusing into the interstitial loops becomes increasingly significant at temperatures $\geq 1523 \text{ K}$ at the level of 1 h anneal. The curves shown in Fig. 8(a,b) agree with the experimental results reported by Ferroni et al. [1] for the bulk material, specifically that the interstitial loops vanished in bulk samples after 1 h annealing at 1673 K. This suggests that vacancy-mediated climb of interstitial loops involving thermal equilibrium vacancies remains the most plausible mechanism explaining their total annihilation in conjunction with the growth of voids observed at 1673 K.

The total annealing times of dislocation loop microstructures interacting with thermal vacancies are given in Fig. 9 together with the data derived from the simulations of the effect of interaction with supersaturated vacancies.

The gradient of thermal vacancy Arrhenius plot $C_0(T)$ yields 5.44 eV for the activation energy of the loop annihilation process, which is close to the activation energy for self-diffusion $E_f + E_m$ in tungsten [79]. The large increase in the activation energy, compared to the case where loops were annihilated by vacancies produced by irradiation, stems from the additional thermal activation associated with the generation of vacancies at external surfaces and surfaces of voids.

3.2.3. Self-climb and vacancy-mediated climb

The coalescence of dislocation loops by self-climb was observed in molybdenum [85], uranium oxide [41], aluminium [47,86], and in ion-irradiated tungsten [1]. Experimental observations refer to two or more loops progressively and steadily drifting towards each other, on the timescale of minutes. The as-irradiated dislocation microstructure of irradiated tungsten is characterized by a relatively homogeneous distribution of interstitial loops, indicating no pronounced clustering of loops. The loops spatially organise themselves into chains and clusters of loops when the microstructure is annealed at relatively low temperatures. In tungsten this occurs in the range of temperatures from 973 K to 1073 K. These chains of dislocation loops and clusters are clearly visible in the bright-field TEM images of microstructures formed after 1 h annealing at 1073 K, see Ref. [1]. This is consistent with simulations showing

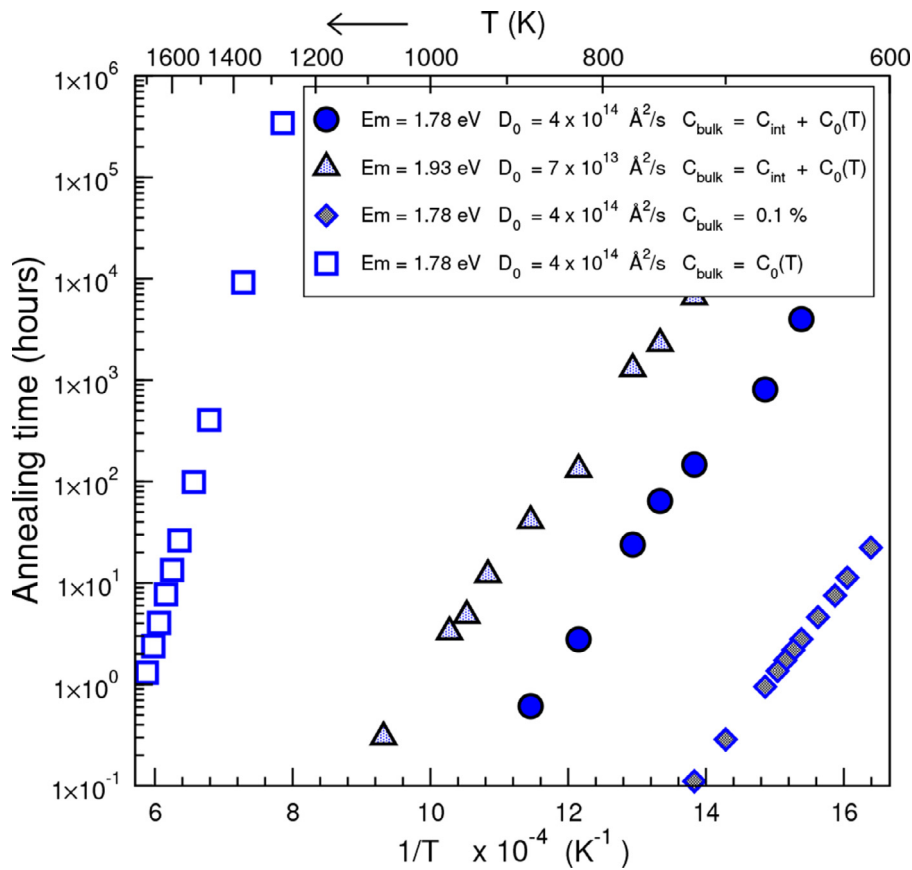


Fig. 9. Arrhenius plot of the annihilation time of an interstitial dislocation loop microstructure of irradiated tungsten, computed assuming the initial thermal (C_0) or irradiation-induced (C_{irr}) concentration of vacancies.

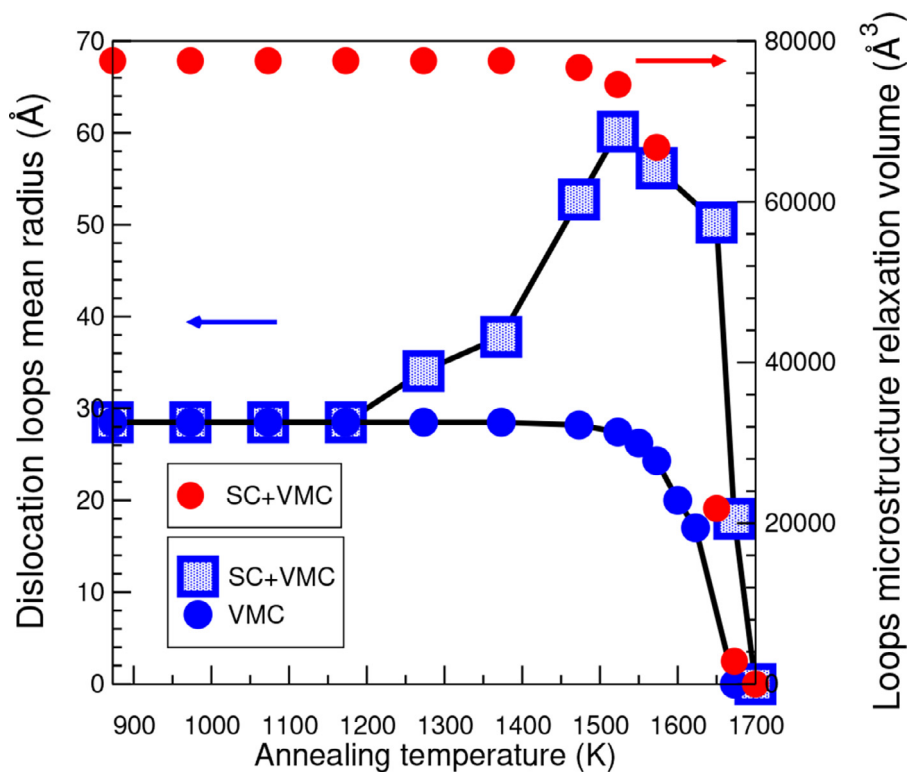


Fig. 10. Variation of the average radius of dislocation loops and the total relaxation volume of loops as functions of temperature following 1 h isochronal annealing in tungsten. The microstructure evolved simultaneously via self (SC) and vacancy-mediated (VMC) climb. For comparison, results of constrained VMC simulations are also shown. In the self-climb process, the activation energy $E_{SC} = 3.58$ eV was used. In the vacancy-mediated climb process, the dislocation loops interact with the field of thermal equilibrium vacancies $C_0(T)$.

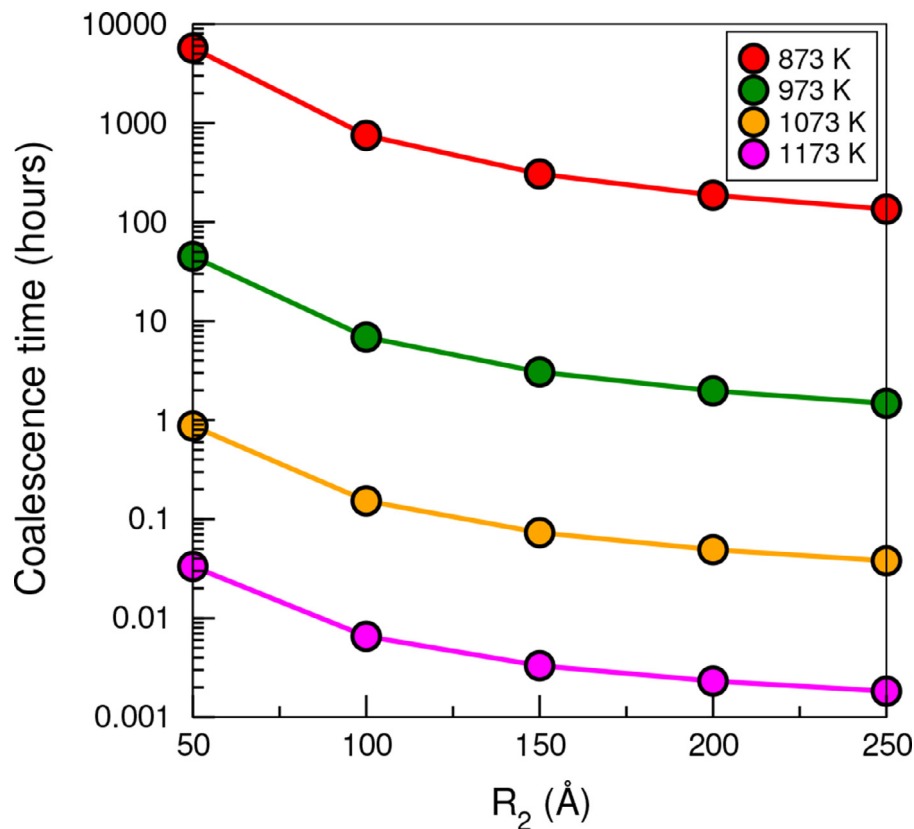


Fig. 11. Coalescence time of two dislocation loops as a function of the radius R_2 of the second loop, evaluated for several temperatures (1 h annealing) in tungsten. The radius of the first loop R_1 is kept constant at 250 Å. The initial distance separating the two loops at their closest point is 20 Å. The self-climb activation energy E_{SC} used in simulations was 3.58 eV.

that elastic interaction between the loops drives their spatial rearrangement and ordering into strings by glide [87,88].

To identify the contribution to the microstructural evolution and coarsening observed in recent experiments on thermal recovery of ion-irradiated tungsten [1], we performed a series of direct dislocation dynamics simulations of the observed effects. A set of ten dislocation loops was randomly positioned as shown in Fig. 12(a). The loops size spans the range from 20 to 50 Å, which approximately corresponds to the observations of as-irradiated specimens [1]. The loops were placed in a common habit plane. This is consistent with the analysis showing that spatial ordering of loops by pure glide, stimulated by elastic interactions, often brings them into the same habit plane. By positioning the loops in the same habit plane, we are able to focus on the role played by self-climb, and explore its effect on the thermal evolution of microstructure.

The loops evolve by self-climb and vacancy-mediated climb at temperatures from 873 K to 1673 K. Simulations were performed using Eq. (14), which describes the evolution of the dislocation loop microstructure evolving via self (SC) and vacancy-mediated (VMC) climb simultaneously.

In simulations, we used the self-climb activation energy derived in Ref. [40], which for the pipe-diffusion along the edge dislocations equals $E_{SC} = 3.58$ eV. Also, we employed the value used in Ref. [40] for the attempt frequency ν for vacancy diffusion in tungsten, which is $1.2 \times 10^{15} \text{ s}^{-1}$ [89]. Similarly to Section 3.2.1, the values of the shear modulus, the Poisson ratio and the lattice parameter used in the simulations were 161 GPa, 0.28 and 3.1795 Å [76], respectively. The Burgers vector of the $1/2(111)$ loops is 2.753 Å. The experimental self-diffusion law for the monovacancies is $D_{SD}^v(T) = 4 \times 10^{14} \exp(-\frac{5.45 \text{ eV}}{k_B T}) \text{ Å}^2/\text{s}$ [79].

Fig. 10 shows the variation of the average radius of loops and evolution of the relaxation volume computed as a function of temperature, assuming the 1 h annealing time. Dislocation microstructure exhibits high sensitivity to the self-climb evolution mode, leading to the coalescence of interacting dislocation loops when the annealing temperature approaches 1273 K ($R_{av} = 34$ Å). It naturally follows that the magnitude of the average loop radius predicted for different annealing temperatures is unique to the example microstructure used here.

The microstructure of loops evolving by self-climb and vacancy-mediated climb progressively coarsens, as illustrated in Fig. 10, which shows that the mean loop radius increases with temperature and is maximum at 1523 K. The SC to VMC transition temperature (SVTT) in tungsten, at which the VMC mechanism starts dominating the evolution of loops interacting with vacancies that are in thermal equilibrium with the environment, is close to 1523 K.

We have also investigated how the pattern of evolution of microstructure depends on the characteristic spatial scale of the distribution of loops. If the radius of all the loops is scaled up twofolds while keeping the distances between the loops the same as in the microstructure simulated above, the coalescence of loops starts at a lower temperature of 1073 K. This in fact is the temperature at which the coalescence of loops was observed in experiment [1].

To investigate further the effect of loop size on the onset of loop coalescence, we evaluated the coalescence time of two large loops with radius = 250 Å at different annealing temperatures. The loops were initially separated by a small distance. No loop coalescence was found after 1 h annealing at temperatures below 1073 K. Considering the large size of the loops and the small initial dis-

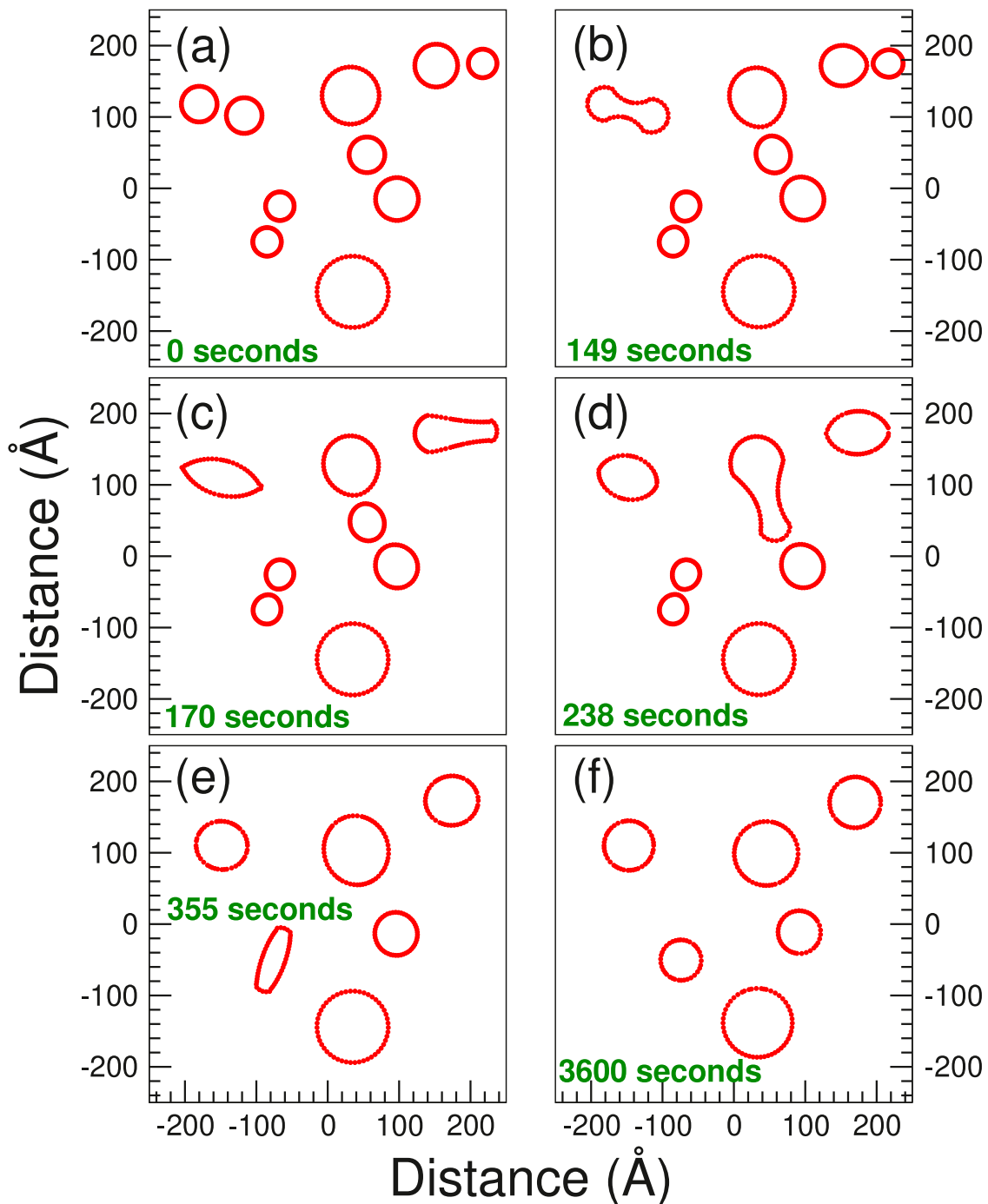


Fig. 12. Snapshots illustrating the time evolution of a dislocation loop microstructure in tungsten at 1373 K simulated assuming the self-climb activation energy of $E_{SC} = 3.58$ eV.

tance separating them, this test shows that regardless of the number density and the spatial distribution of dislocation loops, their coalescence *via* self-climb, observed on the timescale of 1 h and assuming $E_{SC} = 3.58$ eV, can only start above a certain critical temperature, in this specific case ≥ 1073 K. Fig. 11 illustrates the effect of loop size and temperature on the coalescence time between two loops initially separated by a small distance. The radius of the first loop R_1 is kept constant at 250 Å while the radius of the second loop R_2 was allowed to vary between 50 and 250 Å. The initial distance separating the two loops at their closest point is 20 Å. The results shown in Fig. 11 clearly demonstrate that no loop coalescence can occur, as a result of 1 h annealing, below 1073 K.

As opposed to the non-conservative vacancy-mediated climb, where interstitial loops shrink by absorbing vacancies from the medium, in the course of self-climb the loops change their shape and move due to the elastic stress exerted on them by other loops. Loops separated by not very large distances, where one or several of them have appreciable elastic field, tend to attract each other. For example, loop A with the size bigger than loop B exerts an elastic force on loop B. This disturbs the initially uniform self-stress field along the line contour of loop B; consequently, the elastic force profile along the loop B contour becomes non-homogeneous. Loop B then changes its shape to accommodate the effect of elastic force along its contour through self-climb. If loop

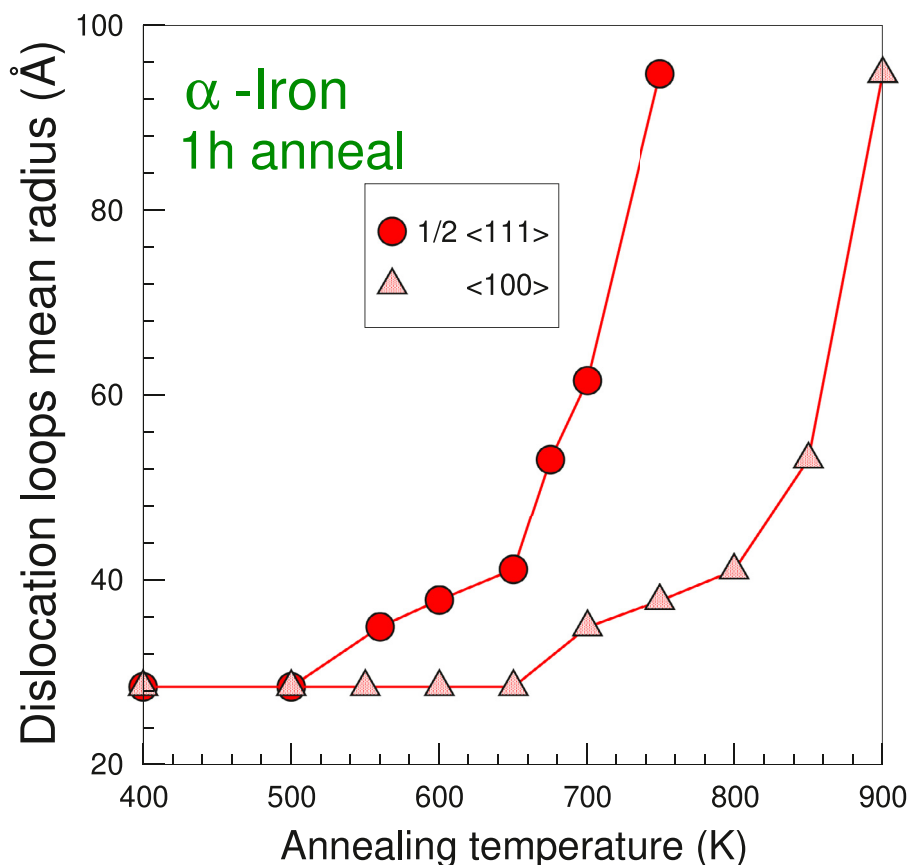


Fig. 13. Variation of the average radius of loops evolving by self-climb in α -iron following an 1 h interval of isochronal annealing. The results were obtained assuming the self-climb activation energy E_{SC} of 1.42 and 1.775 eV for the $1/2\langle 111 \rangle$ and $\langle 100 \rangle$ loops, respectively.

A is much larger than loop B, then loop B will move towards loop A. On the other hand, loops of comparable sizes will move towards each other at similar drift velocities. Upon the coalescence of loops, the newly formed loop features a highly non-uniform shape with a non-uniform self-elastic force profile along its contour. The new loop continuously modifies its shape by self-climb in order to homogenize its self-elastic force profile. Eventually, the loop assumes a stable nearly-circular shape with a uniform self-elastic force profile along its contour.

Fig. 12 shows snapshots of dislocation microstructure simulated at 1373 K assuming $E_{SC} = 3.58$ eV. Depending on the loop size and their initial separation distances, the evolving dislocation loops become distorted by their elastic interaction. As noted above, after coalescence the loops do not immediately relax their shape and remain irregular, depending on the initial configuration of loops involved in the coalescence process. For example, two loops of similar size coalesce into a bone-like dislocation structure (panel b), which progressively evolves into an elliptical-shape (panels c,d), and finally becomes a circle (panel f). Two loops of different size evolve into what loosely resembles a baseball bat (panel c) and gradually develop an elliptical-shape (panel d). All the loops eventually evolve into circles once the distances between the loops become large and elastic interaction between the loops becomes less significant.

3.3. Dislocation self-climb effects in α -iron

In α -iron, interstitial loops with the $1/2\langle 111 \rangle$ and $\langle 100 \rangle$ Burgers vectors can perform one-dimensional stochastic Brownian glide in the direction of their Burgers vector even in the absence of external stress. This was observed in transmission electron micro-

scope (TEM) experiments [90] and molecular dynamics simulations [116,117] [91]. One-dimensional motion of loops was observed even in commercial ferritic steels [92]. Arakawa et al. [75] investigated how two interstitial loops, performing one-dimensional motion along their $1/2\langle 111 \rangle$ and $1/2\langle 11\bar{1} \rangle$ Burgers vectors at 660 K, interacted and coalesced to form a larger loop. In a recent study, Swinburne et al. [40] showed how a conservative core diffusion process can drive the coalescence of interstitial loops in α -iron. However, the effect of dislocation self-climb on the evolution of ensembles of interstitial loops in α -iron and ferritic steels has not yet been explored.

Reactor pressure vessel and structural fusion steels typically contain of the order of 0.01% atomic percent of carbon. Transmission electron microscope observations [75] and simulations [93,94] show that carbon decorates dislocations and dislocation loops, reducing their thermal mobility. It is known that the presence of carbon impurities also affects the evolution of dislocation microstructure [95] and void swelling [96].

Individual carbon impurities become mobile above approximately 350 K, whereas below this temperature the dislocation loops are trapped by carbon impurities or carbon-vacancy complexes. Interstitial dislocation loops absorb vacancies from carbon-vacancy clusters, leaving carbon free to enter the dislocation cores. Above 350 K, interstitial loops interact with migrating carbon, which also reacts with vacancies to form vacancy-carbon clusters [97], some of which remain mobile. For example, VC_2 clusters are mobile above 450 K, see Ref. [97]. Above 600 K, all the vacancy-carbon complexes are dissolved [98]. The binding energy of a carbon atom to a $1/2\langle 111 \rangle$ loop depends on the size of the loop, for example it is close to 0.7 eV for a loop with radius of 10 Å and ~ 0.5 eV for a smaller loop with the radius of 5 Å [99].

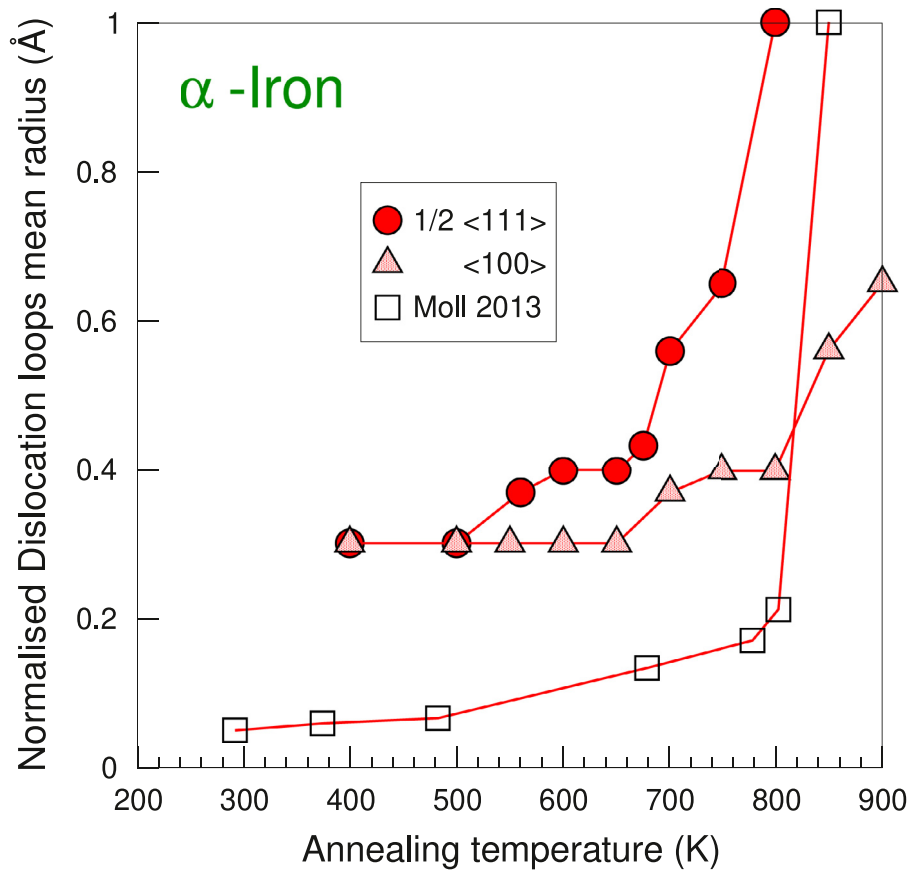


Fig. 14. Variation of the normalised average radius of dislocation loops at various annealing temperatures, determined by simulations (solid circles and triangles) and experiment (squares) in irradiated α -iron [109]. Our simulation data were obtained assuming the self-climb activation energy E_{SC} of 1.42 and 1.775 eV for the $1/2\langle 111 \rangle$ and $\langle 100 \rangle$ loops, respectively.

Whereas it is well established that carbon atoms segregate to dislocations and dislocation loops [94,95], the activation energy for mass transport along a carbon-decorated line edge dislocation remains unknown. In a pure bcc metal, the activation energy for the mass transport along the $1/2\langle 111 \rangle$ and $\langle 100 \rangle$ edge dislocations was determined to be 2 and 2.5 times the vacancy migration barrier, respectively, see Swinburne et al. [40]. The effective migration barrier for a vacancy in the bulk of a carbon-doped α -iron is 1.28 eV [100,101]. This is significantly higher than the migration energy of vacancies in pure bcc Fe, suggesting that pipe-diffusion in iron and steels is strongly affected by the presence of carbon.

To investigate the thermal evolution of the dislocation loop microstructure in pure bcc Fe *via* the self-climb mode, we used an example microstructure consisting of ten loops (see Fig. 12(a)). Simulations were carried using Eq. (12) describing the evolution of the dislocation loop microstructure *via* self-climb.

The temperature-dependent lattice parameter and the corresponding Burgers vector, and the shear modulus, were derived from the experimental data given in Refs. [102,103], respectively. The Poisson ratio of iron is 0.291 [104]. The attempt frequency ν for vacancy diffusion in bcc iron is 10^{13} s^{-1} . The self-climb activation energy E_{SC} for the $1/2\langle 111 \rangle$ and $\langle 100 \rangle$ loops was determined to be 1.42 and 1.775 eV, respectively, as derived from the vacancy migration energy $E_m = 0.71 \text{ eV}$ [105] in bcc Fe.

The microstructure of dislocation loops formed after 1 h isochronal annealing, is shown in Fig. 13. It appears remarkably different for the $1/2\langle 111 \rangle$ and $\langle 100 \rangle$ -type loops. The mean radius of the $1/2\langle 111 \rangle$ loops increases faster than that for the $\langle 100 \rangle$ loops since the former are able to migrate towards each other and coalesce at a greater rate. This difference in the coalescence rate of

$1/2\langle 111 \rangle$ and $\langle 100 \rangle$ loops stems from their different self-climb activation energies, where $E_{SC}(\langle 100 \rangle) = 1.25 \times E_{SC}(1/2\langle 111 \rangle)$. The annealing curves presented in Fig. 13 clearly indicate that the onset temperature at which loops start migrating by self-climb under the effect of elastic interaction is $\sim 550 \text{ K}$ for the $1/2\langle 111 \rangle$ loops and $\sim 700 \text{ K}$ for the $\langle 100 \rangle$ loops, respectively. This prediction is confirmed by in situ TEM observations [106], showing that in pure Fe, the $1/2\langle 111 \rangle$ dislocation microstructure coarsens in the temperature range from 450 to 700 K. Arakawa et al. [106] also showed that the loops vanish above 700 K, an effect that can be attributed to the elimination of loops by thermal vacancies [35,36].

The growth exhibited by the $1/2\langle 111 \rangle$ dislocation microstructure in Fig. 13 not only affects the density of loops but also the morphology of the loops, since the rate of coarsening of the $1/2\langle 111 \rangle$ loops is higher than that of the $\langle 100 \rangle$ loops. This provides evidence that, in addition to the loop glide, the coalescence of the $1/2\langle 111 \rangle$ loops by self-climb might be one of the factors controlling the $1/2\langle 111 \rangle$ to $\langle 100 \rangle$ loop ratio in irradiated iron. Note that the magnitude of the average radius predicted at different annealing temperature for $1/2\langle 111 \rangle$ and $\langle 100 \rangle$ loops in Fig. 13 is unique to the example microstructure used here.

In addition to impurities and alloying elements, a large number of helium atoms can potentially be produced in iron-based materials as a result of transmutation reactions initiated by the high-energy neutrons. Experiments [107] showed that helium atoms segregate to the perimeter of $1/2\langle 111 \rangle$ interstitial dislocation loops in bcc iron. Helium also interacts with vacancy defects, for example, a helium atom forms a bound state with a vacancy, characterised by a high binding energy close to 2.3 eV. The stability of helium-vacancy clusters is controlled by the He-to-vacancy ra-

tio, which for the equilibrium configurations is close to 1.3 [108]. The decoration of $1/2\langle 111 \rangle$ dislocation loops by helium increases the activation energy for loop migration, reducing the diffusivity of loops.

The coarsening of interstitial loops in α -iron during annealing was initially thought to occur *via* vacancy emission and absorption [109,110], similarly to Ostwald ripening. Moll et al. [109] observed the rapid growth of loops at around 850 K. Fig. 14 compares the experimental [109] and simulation data based on the ten loops microstructure, illustrating the change in the loops normalised mean radius during isochronal annealing. To perform a meaningful comparison with experiment, the dwell time in our simulations was set to 1000 s at each temperature. The experimentally observed loop radii corresponding to different temperatures were normalized to the maximum radius observed at 850 K. Similarly, our self-climb data were normalized to the maximum average radius predicted at 800 K. Fig. 14 suggests that in addition to the vacancy emission/absorption argument given in Ref. [109], dislocation self-climb represents an additional evolution mode contributing to the rapid growth of loops observed at high temperatures.

Concluding this section, we would like to comment on the self-climb process occurring within a realistic environment where alloying elements are also present, in addition to iron. EUROFER97 is adopted as the European reference structural steel for the First Wall and the Breeding Blankets of a Demonstration fusion Power Plant (DEMO). It contains a variety of alloying elements including 8.91%Cr, 1.08%W, 0.48%Mn, 0.20%V, 0.14%Ta, 0.12%C, expressed in wt.% [111]. Some of these alloying elements segregate to the dislocation loops formed under irradiation. The presence of these elements within the core of the loop is expected to increase the energy barrier associated with pipe diffusion of atoms along the dislocation lines, and hence affect the dynamics of annealing of radiation defects [112]. For example, a significant number of carbon atoms segregated to the perimeter of a dislocation loop would likely increase the effective activation energy for self-climb. At the same time, it is unlikely that the perimeter of loops would be completely saturated with the alloying elements. Due to the larger activation energy for the self-climb of loops decorated by the alloying elements, the self-climb process in Fe-based alloys is expected to be slower than in pure Fe. In principle, one might employ the elasticity atomic size argument to determine the concentration of alloying elements segregating to the loops, see e.g. the study by Wróbel et al. [113]. This would require extensive molecular statics and Kinetic Monte Carlo simulations to map the energy landscape of pipe-diffusion processes to estimate the self-climb activation energy for the decorated loops. This is outside the scope of this study. The question about the role of the solutes, in particular Cr, and the effect of carbon segregation to the dislocation loop perimeters on the kinetics of self-climb and the corresponding activation energy is a significant topic that warrants further investigation.

4. Conclusions

Discrete dislocation dynamics simulations were performed to investigate the slow dynamics of annealing of ensembles of interstitial dislocation loops as a function of temperature and annealing time. The two processes driving the thermal evolution of defect microstructure, the self-climb of dislocations and vacancy-mediated climb, were modeled using a Green's function-based approach. We found that the vacancy-mediated climb model is able to explain the observed annihilation rates of interstitial loops in irradiated bulk tungsten samples. The onset temperature for self-climb, at which the relatively small size loops start attracting each other to form larger loops through coalescence, is found to be close to 1073 K in tungsten for the 1 h isochronal annealing conditions. In α -iron the onset temperatures for self-climb are close to 550 K

and 700 K for the $1/2\langle 111 \rangle$ and $\langle 100 \rangle$ loops, respectively. These temperature values are expected to be revised upwards if the effect of carbon impurities is taken into account in the simulations. Dislocation self-climb may also contribute to the growth and coarsening of interstitial loops observed during thermal annealing of helium-implanted bcc iron.

CRedit author statement

Both authors have contributed to the manuscript.

Declaration of Competing Interest

The authors declare that they have no known competing financial interests or personal relationships that could have appeared to influence the work reported in this paper.

Acknowledgements

This work has been carried out within the framework of the EUROfusion Consortium and has received funding from the Euratom Research and Training Programme under Grant Agreements no. 633053, 755039, and 101052200 - EUROfusion. The views and opinions expressed herein do not necessarily reflect those of the European Commission. We also acknowledge funding by the RCUK Energy Programme through Grant no. EP/T012250/1.

Appendix A. Numerical implementation

The dislocation lines were discretized so that the dislocation loop microstructure is defined by a set of nodes connected by straight segments, enabling the numerical analysis of dislocation dynamics. We use a node-based approach where nodes are connected by straight line segments. Only a single dislocation configuration is considered at a given time and is used for determining the force acting on a node. The nodes represent the fundamental degrees of freedom of a dislocation line. To handle the topological changes, we applied a set of remeshing rules [114] consisting of multiple criteria, specifically concerning the segment length and the area enclosed by the adjacent segments. Accordingly, the number of nodes was adjusted to reflect the change in the length and line curvature during the simulation. This was essential to refine or coarsen the line representation of the dislocation loops as they evolve in time; for example a line with high local curvature needs to be discretized into finer segments and consequently more nodes, whereas less nodes are needed in a region of low local curvature.

A1. Numerical discretization for the forces acting on loops

In order to evolve the dislocation loop microstructure, the forces acting on the nodes have to be computed. The total elastic force acting on a node i is determined through integrating the Peach–Koehler force $\mathbf{f}_{PK}(\mathbf{x}) = (\boldsymbol{\sigma}(\mathbf{x}) \cdot \mathbf{b}) \times \boldsymbol{\xi}(\mathbf{x})$ where $\boldsymbol{\sigma}(\mathbf{x})$ is the Cauchy stress tensor, weighted by a line shape function $N_i(\mathbf{x})$ [114], along the segments connected to node i i.e. $h-i$ and $i-j$

$$\mathbf{f}_i^{elastic} = \int_h^i \mathbf{f}_{PK}(\mathbf{x}) N_i^{h-i}(\mathbf{x}) dl(\mathbf{x}) + \int_i^j \mathbf{f}_{PK}(\mathbf{x}) N_i^{i-j}(\mathbf{x}) dl(\mathbf{x}), \quad (\text{A.1})$$

The linear shape function $N_i(\mathbf{x})$ is defined in such a way that it assumes non zero values only when \mathbf{x} lies on a segment connected to node i . $N_i(\mathbf{x})$ increases linearly from zero at node h ($\mathbf{x} = \mathbf{r}_h$) to one at node i ($\mathbf{x} = \mathbf{r}_i$) and decreases linearly from one at node i ($\mathbf{x} = \mathbf{r}_i$) to zero at node j ($\mathbf{x} = \mathbf{r}_j$)

$$N_i^{h-i}(\mathbf{x}) = \frac{|\mathbf{x} - \mathbf{r}_h|}{|\mathbf{r}_i - \mathbf{r}_h|}, \quad (\text{A.2})$$

$$N_i^{i-j}(\mathbf{x}) = \frac{|\mathbf{x} - \mathbf{r}_j|}{|\mathbf{r}_i - \mathbf{r}_j|}, \quad (\text{A.3})$$

where \mathbf{r}_h , \mathbf{r}_i and \mathbf{r}_j are the position vectors of nodes h , i and j , respectively.

The Cauchy stress tensor $\boldsymbol{\sigma}(\mathbf{x})$ entering the P-K force $\mathbf{f}_{PK}(\mathbf{x})$ is the total internal stress field at point \mathbf{x} . It is the sum of the stress fields due to all the segments forming the dislocation loop microstructure

$$\boldsymbol{\sigma}(\mathbf{x}) = \sum_{s=t} \boldsymbol{\sigma}(\mathbf{x}; s-t), \quad (\text{A.4})$$

$\boldsymbol{\sigma}(\mathbf{x}; s-t)$ is the stress field at point \mathbf{x} generated by the straight segment connecting nodes s and t , and the sum is taken over all segments in the dislocation microstructure. The non-singular analytic expressions for $\boldsymbol{\sigma}(\mathbf{x}; s-t)$ are derived by Cai et al. [39]. The total elastic force acting on node i in Eq. (A.1) is

$$\mathbf{f}_i^{\text{elastic}} = \int_h^i \left(\sum_{s=t} \boldsymbol{\sigma}(\mathbf{x}; s-t) \right) \cdot \mathbf{b} \times \boldsymbol{\xi}(\mathbf{x}) N_i^{h-i}(\mathbf{x}) dl(\mathbf{x}) + \int_i^j \left(\sum_{s=t} \boldsymbol{\sigma}(\mathbf{x}; s-t) \right) \cdot \mathbf{b} \times \boldsymbol{\xi}(\mathbf{x}) N_i^{i-j}(\mathbf{x}) dl(\mathbf{x}), \quad (\text{A.5})$$

The dislocation core energy also contributes to the nodal forces and total energy. Obtaining the core force per unit length is not straightforward. Instead, we derive the core force acting on node i from the the core energy of the straight segments connected to i . In principle, the core energy per unit length of the dislocation line at point \mathbf{x} , $E_c(\mathbf{x})$, can be obtained using first-principles or atomistic methods as a function of $\theta(\mathbf{x})$, the angle between the line direction and the Burgers vector, known as the character angle. Alternatively, an approximate analytical expression describing $E_c(\mathbf{x})$ can be employed. According to the deWit and Koehler model [115], the core energy per unit length is given by

$$E_c(\mathbf{x}) = \frac{\mu b^2}{4\pi(1-\nu)} \ln\left(\frac{r_\infty}{r_c}\right) [1 - \nu \cos^2 \theta(\mathbf{x})], \quad (\text{A.6})$$

The core energy of segment $h-i$ can then be determined by integrating $E_c(\mathbf{x})$ as

$$E_c(h-i) = \int_h^i E_c(\mathbf{x}) dl(\mathbf{x}) = \frac{\mu b^2}{4\pi(1-\nu)} \ln\left(\frac{r_\infty}{r_c}\right) [1 - \nu \cos^2 \theta^{hi}] |\mathbf{r}_i - \mathbf{r}_h|, \quad (\text{A.7})$$

The contribution of segment $h-i$ to the core force at node i is

$$\mathbf{f}_i^{\text{core}}(h-i) = - \frac{\partial E_c(h-i)}{\partial \mathbf{r}_i}, \quad (\text{A.8})$$

For convenience, knowing that $\cos \theta^{hi} = \hat{\mathbf{b}} \cdot \boldsymbol{\xi}^{hi} = \hat{\mathbf{b}} \cdot \frac{(\mathbf{r}_i - \mathbf{r}_h)}{|\mathbf{r}_i - \mathbf{r}_h|}$ where $\hat{\mathbf{b}} = \frac{\mathbf{b}}{|\mathbf{b}|}$ is the Burgers unit vector, Eq. (A.7) can be written as

$$E_c(h-i) = \frac{\mu b^2}{4\pi(1-\nu)} \ln\left(\frac{r_\infty}{r_c}\right) \left[|\mathbf{r}_i - \mathbf{r}_h| - \nu \frac{(\hat{\mathbf{b}} \cdot (\mathbf{r}_i - \mathbf{r}_h))^2}{|\mathbf{r}_i - \mathbf{r}_h|} \right], \quad (\text{A.9})$$

Then

$$\begin{aligned} \mathbf{f}_i^{\text{core}}(h-i) &= \frac{\mu b^2}{4\pi(1-\nu)} \ln\left(\frac{r_\infty}{r_c}\right) \left[2\nu (\hat{\mathbf{b}} \cdot \boldsymbol{\xi}^{hi}) \hat{\mathbf{b}} - (1 + \nu (\hat{\mathbf{b}} \cdot \boldsymbol{\xi}^{hi})^2) \boldsymbol{\xi}^{hi} \right] \\ &= \frac{\mu b^2}{4\pi(1-\nu)} \ln\left(\frac{r_\infty}{r_c}\right) \left[2\nu \cos \theta^{hi} \hat{\mathbf{b}} - (1 + \nu \cos^2 \theta^{hi}) \boldsymbol{\xi}^{hi} \right], \end{aligned} \quad (\text{A.10})$$

Similarly, the contribution of segment $i-j$ to the core force at node i can be calculated as

$$\mathbf{f}_i^{\text{core}}(i-j) = - \frac{\partial E_c(i-j)}{\partial \mathbf{r}_i} = \frac{\mu b^2}{4\pi(1-\nu)} \ln\left(\frac{r_\infty}{r_c}\right) \left[-2\nu \cos \theta^{ij} \hat{\mathbf{b}} + (1 + \nu \cos^2 \theta^{ij}) \boldsymbol{\xi}^{ij} \right], \quad (\text{A.11})$$

The total core force at node i is then

$$\mathbf{f}_i^{\text{core}} = \frac{\mu b^2}{4\pi(1-\nu)} \ln\left(\frac{r_\infty}{r_c}\right) \left\{ 2\nu (\cos \theta^{hi} - \cos \theta^{ij}) \hat{\mathbf{b}} - \boldsymbol{\xi}^{hi} + \boldsymbol{\xi}^{ij} - \nu (\boldsymbol{\xi}^{hi} \cos^2 \theta^{hi} - \boldsymbol{\xi}^{ij} \cos^2 \theta^{ij}) \right\}, \quad (\text{A.12})$$

The total force, acting on each node, needed to evolve the dislocation loop microstructure

$$\mathbf{f}_i = \mathbf{f}_i^{\text{elastic}} + \mathbf{f}_i^{\text{core}}, \quad (\text{A.13})$$

is evaluated from Eqs. (A.5) to (A.12).

To model the climb evolution, the total force \mathbf{f}_i is projected along the climb direction at node i , hence $f_i^{\text{cl}} = \mathbf{f}_i \cdot \mathbf{n}_i$. Note that the climb force F^{cl} involved in the vacancy-mediated climb VMC and self-climb SC Eqs. (4)–(6) and (12), respectively, is the force per unit length acting on the line. The climb force per unit length, needed to evaluate the VMC and SC climb velocities, can be determined as

$$F_i^{\text{cl}} = \frac{f_i^{\text{cl}}}{\mathcal{L}_i}, \quad (\text{A.14})$$

where $\mathcal{L}_i = \frac{|\mathbf{r}_i - \mathbf{r}_h| + |\mathbf{r}_j - \mathbf{r}_i|}{2}$.

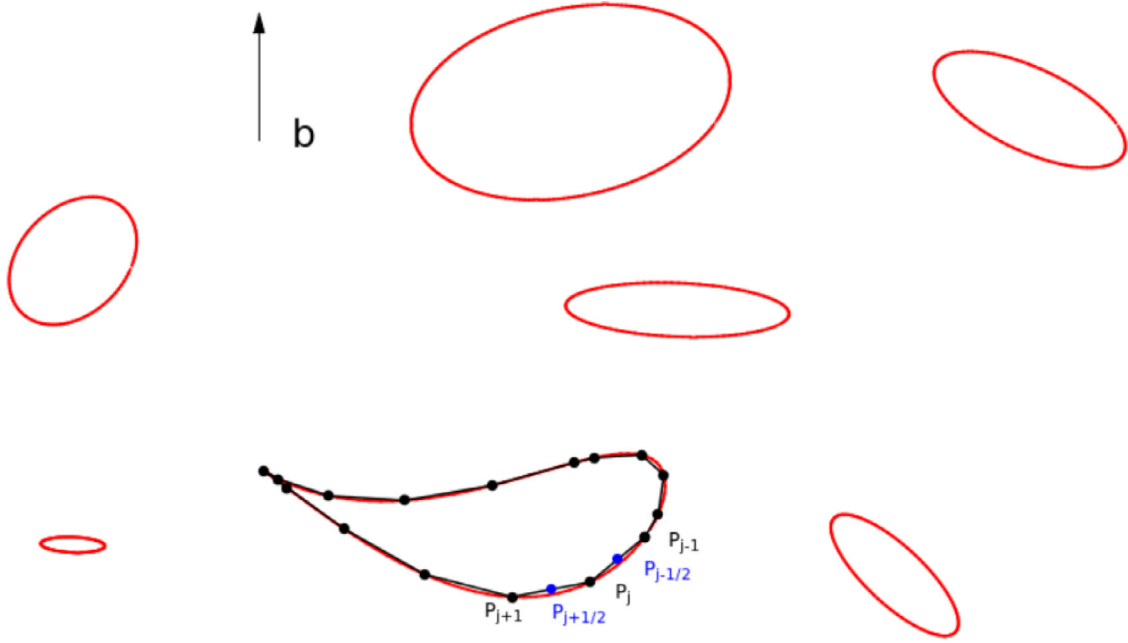


Fig. A.15. A dislocation loop microstructure example, showing an arbitrarily shaped loop numerically discretized into piece-wise straight segments connected by nodes. $P_{j-\frac{1}{2}}$ and $P_{j+\frac{1}{2}}$ are the midpoints of the dislocation segments $P_{j-1}P_j$ and P_jP_{j+1} , respectively. \mathbf{b} is the Burgers vector of the dislocation loop microstructure.

A2. Numerical discretization for vacancy-mediated climb velocities

Gu et al. [34] presented an implementation of vacancy mediated-climb VMC for a two dimensional 2D prismatic loop. Here, we generalize the implementation for an ensemble of 3D arbitrarily-shaped loops where dislocation segments have mixed character; and include the core force contribution to the climb force.

The Green's function formulation of the non-local VMC velocity given by Eq. (4) is

$$\int_{\Gamma} \frac{b_e(\mathbf{x}') v_{cl}(\mathbf{x}')}{|\mathbf{x}_{\Gamma} - \mathbf{x}'|} dl(\mathbf{x}') = 4\pi D_v [C_{bulk} - C_{\Gamma}(\mathbf{x}_{\Gamma})], \quad (\text{A.15})$$

We showed earlier that every dislocation loop is discretized into a set of piece-wise straight segments connected by nodes, as shown in Fig. A.15. We also presented how we calculate the climb force F_i^{cl} at node i . Let's note here that the above integral Eq. (A.15) holds at each node $i = 1, 2, 3, \dots, N$, where N is the total number of nodes in the dislocation loop microstructure, and $\mathbf{x}_{\Gamma} = \mathbf{x}_i$. For closed dislocation loops, the left-hand side of the integral Eq. (A.15) can be discretized as

$$\begin{aligned} & \int_{\Gamma} \frac{b_e(\mathbf{x}') v_{cl}(\mathbf{x}')}{|\mathbf{x}_{\Gamma} - \mathbf{x}'|} dl(\mathbf{x}') \\ &= \sum_{j=1}^N \left\{ \int_{P_{j-\frac{1}{2}}}^{P_j} \frac{b_e(\mathbf{x}') v_{cl}(\mathbf{x}')}{|\mathbf{x}_i - \mathbf{x}'|} dl(\mathbf{x}') + \int_{P_j}^{P_{j+\frac{1}{2}}} \frac{b_e(\mathbf{x}') v_{cl}(\mathbf{x}')}{|\mathbf{x}_i - \mathbf{x}'|} dl(\mathbf{x}') \right\} \\ &= \sum_{j=1}^N v_{cl}^j \left\{ b_e^{j-1,j} \int_{P_{j-\frac{1}{2}}}^{P_j} \frac{dl(\mathbf{x}')}{|\mathbf{x}_i - \mathbf{x}'|} + b_e^{j,j+1} \int_{P_j}^{P_{j+\frac{1}{2}}} \frac{dl(\mathbf{x}')}{|\mathbf{x}_i - \mathbf{x}'|} \right\}, \quad (\text{A.16}) \end{aligned}$$

where P_j denotes the spatial coordinates (x_j, y_j, z_j) of the node j ; similarly P_{j-1} and P_{j+1} denote those of nodes $j-1$ and $j+1$, respectively. $P_{j-\frac{1}{2}}$ and $P_{j+\frac{1}{2}}$ are the midpoints of the dislocation segments $P_{j-1}P_j$ and P_jP_{j+1} , respectively, as shown in Fig. A.15. $b_e^{j-1,j}$ and $b_e^{j,j+1}$ are the edge components of the Burgers vectors of the segments $P_{j-1}P_j$ and P_jP_{j+1}

$$b_e^{j-1,j} = \|\xi^{j-1,j} \times \mathbf{b}\|$$

$$b_e^{j,j+1} = \|\xi^{j,j+1} \times \mathbf{b}\|, \quad (\text{A.17})$$

Let's designate the coefficient

$$a_{ij} = b_e^{j-1,j} \int_{P_{j-\frac{1}{2}}}^{P_j} \frac{dl(\mathbf{x}')}{|\mathbf{x}_i - \mathbf{x}'|} + b_e^{j,j+1} \int_{P_j}^{P_{j+\frac{1}{2}}} \frac{dl(\mathbf{x}')}{|\mathbf{x}_i - \mathbf{x}'|}, \quad (\text{A.18})$$

Hence, the final form of the integral Eq. (A.15) in its discretized form is a matrix equation

$$\sum_{j=1}^N a_{ij} v_{cl}^j = 4\pi D_v [C_{bulk} - C_{\Gamma}(\mathbf{x}_i)], \quad (\text{A.19})$$

When $j = i$ ($\mathbf{x}' = \mathbf{x}_i$), the integrands in Eq. (A.18) diverge logarithmically. In order to eliminate this singularity, one can consider a boundary (r_c) around the node i to be excluded from the integration [31], therefore

$$a_{ii} = b_e^{i-1,i} \int_{P_{i-\frac{r_c}{2}}}^{P_i} \frac{dl(\mathbf{x}')}{|\mathbf{x}_i - \mathbf{x}'|} + b_e^{i,i+1} \int_{P_i}^{P_{i+\frac{r_c}{2}}} \frac{dl(\mathbf{x}')}{|\mathbf{x}_i - \mathbf{x}'|}, \quad (\text{A.20})$$

where $P_{i-\frac{r_c}{2}}$ is a point lying on the segment $P_{i-1}P_i$ and separated by a distance $r_c/2$ from node i . Similarly, $P_{i+\frac{r_c}{2}}$ is a point lying on the segment P_iP_{i+1} and separated by a distance $r_c/2$ from node i .

The integrated form of Eq. (A.20) is

$$a_{ii} = b_e^{i-1,i} \ln\left(\frac{|\mathbf{x}_i - \mathbf{x}_{i-1}|}{r_c}\right) + b_e^{i,i+1} \ln\left(\frac{|\mathbf{x}_{i+1} - \mathbf{x}_i|}{r_c}\right), \quad (\text{A.21})$$

For $j \neq i$,

$$a_{ij} = b_e^{j-1,j} I_1 + b_e^{j,j+1} I_2, \quad (\text{A.22})$$

where

$$I_k = \ln \left[\frac{\sqrt{A_k^2 + 4A_k B_k + 4A_k C + A_k + 2B_k}}{2(\sqrt{A_k C} + B_k)} \right] \quad (\text{A.23})$$

If $\sqrt{A_k C} + B_k \neq 0$

and

$$I_k = \ln \left[\frac{2(\sqrt{A_k C} - B_k)}{\sqrt{A_k^2 + 4A_k B_k + 4A_k C - A_k - 2B_k}} \right]$$

$$\text{If } \sqrt{A_k C} + B_k = 0,$$

for $k = 1, 2$.

Note that

$$A_1 = |\mathbf{x}_j - \mathbf{x}_{j-1}|^2 \quad (\text{A.24})$$

$$A_2 = |\mathbf{x}_{j+1} - \mathbf{x}_j|^2$$

$$B_1 = (\mathbf{x}_j - \mathbf{x}_{j-1}) \cdot (\mathbf{x}_i - \mathbf{x}_j)$$

$$B_2 = (\mathbf{x}_{j+1} - \mathbf{x}_j) \cdot (\mathbf{x}_i - \mathbf{x}_j)$$

$$C = |\mathbf{x}_i - \mathbf{x}_j|^2.$$

The system of linear equations presented in Eq. (A.19) can be solved numerically for the VMC velocity v_{cl}^i at all the nodes in the dislocation loop microstructure.

References

- [1] F. Ferroni, X. Yi, K. Arakawa, S.P. Fitzgerald, P.D. Edmondson, S.G. Roberts, High temperature annealing of ion irradiated tungsten, *Acta Mater.* 90 (2015) 380–393, doi:10.1016/j.actamat.2015.01.067.
- [2] E. Gaganidze, H.-C. Schneider, B. Dafferner, J. Aktaa, Embrittlement behavior of neutron irradiated RAFM steels, *J. Nucl. Mater.* 367–370 (2007) 81–85, doi:10.1016/j.jnucmat.2007.03.163.
- [3] F.A. Garner, Radiation-induced damage in austenitic structural steels used in nuclear reactors, in: R.J. Konings, R.E. Stoller (Eds.), *Comprehensive Nuclear Materials*, vol. 3, second ed., Elsevier, Oxford, 2020, pp. 57–168, doi:10.1016/B978-0-12-803581-8.12067-3.
- [4] S.J. Zinkle, N.M. Ghoniem, Operating temperature windows for fusion reactor structural materials, *Fusion Eng. Des.* 51–52 (2000) 55–71, doi:10.1016/S0920-3796(00)00320-3.
- [5] *Structural Alloys for Nuclear Energy Applications*, G.R. Odette, S.J. Zinkle (Eds.), Elsevier, 2019, doi:10.1016/B978-0-12-397046-6.09991-3.
- [6] S.J. Zinkle, L.L. Snead, Designing radiation resistance in materials for fusion energy, *Annu. Rev. Mater. Res.* 44 (2014) 241–267, doi:10.1146/annurev-matsci-070813-113627.
- [7] G. Pintsuk, E. Diegele, S.L. Dudarev, M. Gorley, J. Henry, J. Reiser, M. Rieth, European materials development: results and perspective, *Fusion Eng. Des.* 146 (2019) 1300–1307, doi:10.1016/j.fusengdes.2019.02.063.
- [8] M. Kiritani, Microstructure evolution during irradiation, *J. Nucl. Mater.* 216 (1994) 220–264, doi:10.1016/0022-3115(94)90014-0.
- [9] C.H. Woo, B.N. Singh, The concept of production bias and its possible role in defect accumulation under cascade damage conditions, *Phys. Status Solidi (b)* 159 (1990) 609–616, doi:10.1002/pssb.2221590210.
- [10] D.R. Mason, S. Das, P.M. Derlet, S.L. Dudarev, A.J. London, H. Yu, N.W. Phillips, D. Yang, K. Mizohata, R. Xu, F. Hofmann, Observation of transient and asymptotic driven structural states of tungsten exposed to radiation, *Phys. Rev. Lett.* 125 (2020) 225503, doi:10.1103/PhysRevLett.125.225503.
- [11] P.M. Derlet, S.L. Dudarev, Microscopic structure of a heavily irradiated material, *Phys. Rev. Mater.* 4 (2020) 023605, doi:10.1103/PhysRevMaterials.4.023605.
- [12] A. Chartier, M.C. Marinica, Rearrangement of interstitial defects in alpha-Fe under extreme condition, *Acta Mater.* 180 (2019) 141–148, doi:10.1016/j.actamat.2019.09.007.
- [13] M.C. Marinica, F. Willaime, J.P. Crocombette, Irradiation-induced formation of nanocrystallites with C15 laves phase structure in bcc Iron, *Phys. Rev. Lett.* 108 (2012) 025501–025505, doi:10.1103/PhysRevLett.108.025501.
- [14] R. Alexander, M.-C. Marinica, L. Proville, F. Willaime, K. Arakawa, M.R. Gilbert, S.L. Dudarev, Ab initio scaling laws for the formation energy of nanosized interstitial defect clusters in iron, tungsten, and vanadium, *Phys. Rev. B* 94 (2016) 024103, doi:10.1103/PhysRevB.94.024103.
- [15] P.-W. Ma, D.R. Mason, S.L. Dudarev, Multiscale analysis of dislocation loops and voids in tungsten, *Phys. Rev. Mater.* 4 (2020) 103609, doi:10.1103/PhysRevMaterials.4.103609.
- [16] A.D. Brailsford, R. Bullough, The theory of sink strengths, *Philos. Trans. R. Soc. Lond.* 302 (1981) 87–137, doi:10.1098/rsta.1981.0158.
- [17] P.W. Ma, S.L. Dudarev, Universality of point defect structure in body-centered cubic metals, *Phys. Rev. Mater.* 3 (2019) 013605, doi:10.1103/PhysRevMaterials.3.013605.
- [18] D.R. Mason, D. Nguyen-Manh, M.-C. Marinica, R. Alexander, A.E. Sand, S.L. Dudarev, Relaxation volumes of microscopic and mesoscopic irradiation-induced defects in tungsten, *J. Appl. Phys.* 126 (2019) 075112, doi:10.1063/1.5094852.
- [19] P.-W. Ma, S.L. Dudarev, Nonuniversal structure of point defects in face-centered cubic metals, *Phys. Rev. Mater.* 5 (2021) 013601, doi:10.1103/PhysRevMaterials.5.013601.
- [20] S.L. Dudarev, Density functional theory models for radiation damage, *Annu. Rev. Mater. Res.* 43 (2013) 35–61, doi:10.1146/annurev-matsci-071312-121626.
- [21] W. Cai, W.D. Nix, *Imperfections in Crystalline Solids*, Cambridge University Press, England, UK, 2016.
- [22] Y. Kraftmakher, Equilibrium vacancies and thermophysical properties of metals, *Phys. Rep.* 299 (1998) 79–188, doi:10.1016/S0370-1573(97)00082-3.
- [23] Y. Kraftmakher, *Equilibrium Point Defects and Thermophysical Properties of Metals*, World Scientific, Singapore, 2000.
- [24] A. Mannheim, J.A.W. van Dommelen, M.G.D. Geers, Long-term microstructural evolution of tungsten under heat and neutron loads, *Comput. Mater. Sci.* 170 (2019) 109146, doi:10.1016/j.commatsci.2019.109146.
- [25] J. Narayan, J. Washburn, Self-climb of dislocation loops in magnesium oxide, *Philos. Mag.* 26 (1972) 1179–1190, doi:10.1080/14786437208227372.
- [26] S.J. Zinkle, Radiation-induced effects on microstructure, in: R.J. Konings (Ed.), *Comprehensive Nuclear Materials*, Elsevier, Oxford, 2012, pp. 65–98, doi:10.1016/B978-0-08-056033-5.00003-3.
- [27] R. Vandervoort, J. Washburn, On the stability of the dislocation substructure in quenched aluminium, *Philos. Mag.* 5 (1960) 24–29, doi:10.1080/14786436008241197.
- [28] J. Silcox, M.J. Whelan, Direct observations of the annealing of prismatic dislocation loops and of climb of dislocations in quenched aluminium, *Philos. Mag.* 5 (1960) 1–23, doi:10.1080/14786436008241196.
- [29] C.A. Johnson, The growth of prismatic dislocation loops during annealing, *Philos. Mag.* 5 (1960) 1255–1265, doi:10.1080/14786436008238338.
- [30] C. McElfresh, Y. Cui, S.L. Dudarev, G. Po, J. Marian, Discrete stochastic model of point defect–dislocation interaction for simulating dislocation climb, *Int. J. Plast.* 136 (2021) 102848, doi:10.1016/j.ijplas.2020.102848.
- [31] P.M. Anderson, J.P. Hirth, J. Lothe, *Theory of Dislocations*, Cambridge University Press, New York, 2017.
- [32] P.-W. Ma, S.L. Dudarev, Effect of stress on vacancy formation and migration in body-centered-cubic metals, *Phys. Rev. Mater.* 3 (2019) 063601, doi:10.1103/PhysRevMaterials.3.063601.
- [33] D. Mordehai, E. Clouet, M. Fivel, M. Verdier, Introducing dislocation climb by bulk diffusion in discrete dislocation dynamics, *Philos. Mag.* 88 (2008) 899–925, doi:10.1080/14786430801992850.
- [34] Y. Gu, Y. Xiang, S.S. Quek, D.J. Srolovitz, Three-dimensional formulation of dislocation climb, *J. Mech. Phys. Solids* 83 (2015) 319–337, doi:10.1016/j.jmps.2015.04.002.
- [35] I. Rovelli, S.L. Dudarev, A.P. Sutton, Non-local model for diffusion-mediated dislocation climb and cavity growth, *J. Mech. Phys. Solids* 103 (2017) 121–141, doi:10.1016/j.jmps.2017.03.008.
- [36] I. Rovelli, S.L. Dudarev, A.P. Sutton, Statistical model for diffusion-mediated recovery of dislocation and point-defect microstructure, *Phys. Rev. E* 98 (2018) 043002, doi:10.1103/PhysRevE.98.043002.
- [37] N.L. Peterson, Self-diffusion in pure metals, *J. Nucl. Mater.* 67–70 (1978) 3–37, doi:10.1016/0022-3115(78)90234-9.
- [38] S.L. Dudarev, P.-W. Ma, Elastic fields, dipole tensors, and interaction between self-interstitial atom defects in bcc transition metals, *Phys. Rev. Mater.* 2 (2018) 033602, doi:10.1103/PhysRevMaterials.2.033602.
- [39] W. Cai, A. Arsenlis, C.R. Weinberger, V.V. Bulatov, A non-singular continuum theory of dislocations, *J. Mech. Phys. Solids* 54 (2006) 561–587, doi:10.1016/j.jmps.2005.09.005.
- [40] T.D. Swinburne, K. Arakawa, H. Mori, H. Yasuda, M. Isshiki, K. Mimura, M. Uchikoshi, S.L. Dudarev, Fast, vacancy-free climb of prismatic dislocation loops in bcc metals, *Sci. Rep.* 6 (2016) 30596, doi:10.1038/srep30599.
- [41] J.A. Turnbull, The coalescence of dislocation loops by self climb, *Philos. Mag.* 21 (1970) 83–94, doi:10.1080/14786437008238398.
- [42] X. Niu, T. Luo, J. Lu, Y. Xiang, Dislocation climb models from atomistic scheme to dislocation dynamics, *J. Mech. Phys. Solids* 99 (2017) 242–258, doi:10.1016/j.jmps.2016.11.012.
- [43] X. Niu, Y. Gu, Y. Xiang, Dislocation dynamics formulation for self-climb of dislocation loops by vacancy pipe diffusion, *Int. J. Plast.* 120 (2019) 262–277, doi:10.1016/j.ijplas.2019.05.002.
- [44] F. Liu, A.C. Cocks, E. Tarleton, A new method to model dislocation self-climb dominated by core diffusion, *J. Mech. Phys. Solids* 135 (2020) 103783, doi:10.1016/j.jmps.2019.103783.
- [45] F. Liu, A.C.F. Cocks, S.P.A. Gill, E. Tarleton, An improved method to model dislocation self-climb, *Model. Simul. Mater. Sci. Eng.* 28 (2020) 055012, doi:10.1088/1361-651x/ab81a8.
- [46] X. Niu, Y. Xiang, X. Yan, Phase field model for self-climb of prismatic dislocation loops by vacancy pipe diffusion, *Int. J. Plast.* 141 (2021) 102977, doi:10.1016/j.ijplas.2021.102977.
- [47] F. Kroupa, P.B. Price, ‘conservative climb’ of a dislocation loop due to its interaction with an edge dislocation, *Philos. Mag.* 6 (1961) 243–247, doi:10.1080/14786436108243313.
- [48] T. Okita, S. Hayakawa, M. Itakura, M. Aichi, S. Fujita, K. Suzuki, Conservative climb motion of a cluster of self-interstitial atoms toward an edge dislocation in BCC-Fe, *Acta Mater.* 118 (2016) 342–349, doi:10.1016/j.actamat.2016.08.003.
- [49] H. Mehrer, N. Stolica, N.A. Stolwijk, 2.2.13 Aluminum group metals: Datasheet from Landolt–Börnstein - Group III Condensed Matter Volume 26: Diffusion in Solid Metals and Alloys, Springer-Verlag, 1990. 10.1007/10390457_22
- [50] S. Dais, R. Messer, A. Seeger, Nuclear-magnetic-resonance study of self-diffusion in aluminium, in: *Vacancies and Interstitials in Metals and Alloys*, in: *Materials Science Forum*, vol. 15, Trans Tech Publications Ltd, 1987, pp. 419–424. 10.4028/www.scientific.net/MSF.15-18.419
- [51] N. Sandberg, B. Magyari-Köpe, T.R. Mattsson, Self-diffusion rates in Al from combined first-principles and model-potential calculations, *Phys. Rev. Lett.* 89 (2002) 065901, doi:10.1103/PhysRevLett.89.065901.

- [52] D. Gerlich, E. Fisher, The high temperature elastic moduli of aluminum, *J. Phys. Chem. Solids* 30 (5) (1969) 1197–1205, doi:[10.1016/0022-3697\(69\)90377-1](https://doi.org/10.1016/0022-3697(69)90377-1).
- [53] A. Breidi, S. Fries, M. Palumbo, A. Ruban, First-principles modeling of energetic and mechanical properties of Ni–Cr, Ni–Re and Cr–Re random alloys, *Comput. Mater. Sci.* 117 (2016) 45–53, doi:[10.1016/j.commatsci.2016.01.020](https://doi.org/10.1016/j.commatsci.2016.01.020).
- [54] G. Langelaan, S. Saimoto, Thermal expansion measurement of pure aluminum using a very low thermal expansion heating stage for X-ray diffraction experiments, *Rev. Sci. Instrum.* 70 (1999) 3413–3417, doi:[10.1063/1.1149928](https://doi.org/10.1063/1.1149928).
- [55] J. Roth, E. Tsitrone, A. Loarte, T. Loarer, G. Counsell, R. Neu, V. Philipps, S. Brezinsek, M. Lehnen, P. Coad, C. Grisolia, K. Schmid, K. Krieger, A. Kallenbach, B. Lipschultz, R. Doerner, R. Causey, V. Alimov, W. Shu, O. Ogorodnikova, A. Kirschner, G. Federici, A. Kukushkin, Recent analysis of key plasma wall interactions issues for ITER, *J. Nucl. Mater.* 390–391 (2009) 1–9, doi:[10.1016/j.jnucmat.2009.01.037](https://doi.org/10.1016/j.jnucmat.2009.01.037). Proceedings of the 18th International Conference on Plasma-Surface Interactions in Controlled Fusion Device
- [56] H. Bolt, V. Barabash, W. Krauss, J. Linke, R. Neu, S. Suzuki, N. Yoshida, A.U. Team, Materials for the plasma-facing components of fusion reactors, *J. Nucl. Mater.* 329–333 (2004) 66–73, doi:[10.1016/j.jnucmat.2004.04.005](https://doi.org/10.1016/j.jnucmat.2004.04.005). Proceedings of the 11th International Conference on Fusion Reactor Materials (ICFRM-11)
- [57] A. Giannattasio, Z. Yao, E. Tarleton, S. Roberts, Brittle-ductile transitions in polycrystalline tungsten, *Philos. Mag.* 90 (2010) 3947–3959, doi:[10.1080/14786435.2010.502145](https://doi.org/10.1080/14786435.2010.502145).
- [58] X. Hu, T. Koyanagi, M. Fukuda, N.K. Kumar, L.L. Snead, B.D. Wirth, Y. Katoh, Irradiation hardening of pure tungsten exposed to neutron irradiation, *J. Nucl. Mater.* 480 (2016) 235–243, doi:[10.1016/j.jnucmat.2016.08.024](https://doi.org/10.1016/j.jnucmat.2016.08.024).
- [59] D.E.J. Armstrong, P.D. Edmondson, S.G. Roberts, Effects of sequential tungsten and helium ion implantation on nano-indentation hardness of tungsten, *Appl. Phys. Lett.* 102 (2013) 251901, doi:[10.1063/1.4811825](https://doi.org/10.1063/1.4811825).
- [60] F. Hofmann, D.R. Mason, J.K. Eliason, A.A. Maznev, K.A. Nelson, S.L. Dudarev, Non-contact measurement of thermal diffusivity in ion-implanted nuclear materials, *Sci. Rep.* 5 (2015) 15042, doi:[10.1038/srep16042](https://doi.org/10.1038/srep16042).
- [61] H. Bolt, V. Barabash, G. Federici, J. Linke, A. Loarte, J. Roth, K. Sato, Plasma facing and high heat flux materials – needs for ITER and beyond, *J. Nucl. Mater.* 307–311 (2002) 43–52, doi:[10.1016/S0022-3115\(02\)01175-3](https://doi.org/10.1016/S0022-3115(02)01175-3).
- [62] M.W. Thompson, The damage and recovery of neutron irradiated tungsten, *Philos. Mag.* 5 (1960) 278–296, doi:[10.1080/14786436008235842](https://doi.org/10.1080/14786436008235842).
- [63] D.R. Mason, X. Yi, M.A. Kirk, S.L. Dudarev, Elastic trapping of dislocation loops in cascades in ion-irradiated tungsten foils, *J. Phys.* 26 (2014) 375701, doi:[10.1088/0953-8984/26/37/375701](https://doi.org/10.1088/0953-8984/26/37/375701).
- [64] J. Heikinheimo, K. Mizohata, J. Räsänen, T. Ahlgren, P. Jalkanen, A. Lahtinen, N. Catarino, E. Alves, F. Tuomisto, Direct observation of mono-vacancy and self-interstitial recovery in tungsten, *APL Mater.* 7 (2019) 021103, doi:[10.1063/1.5082150](https://doi.org/10.1063/1.5082150).
- [65] L.K. Keys, J. Moteff, Neutron irradiation and defect recovery of tungsten, *J. Nucl. Mater.* 34 (1970) 260–280, doi:[10.1016/0022-3115\(70\)90193-5](https://doi.org/10.1016/0022-3115(70)90193-5).
- [66] M.I. Zakharova, V.A. Solov'ev, V.N. Bykov, High-temperature stages of the annealing of radiation defects in refractory BCC metals, *Sov. At. Energy* 38 (1975) 101–104, doi:[10.1007/BF01208865](https://doi.org/10.1007/BF01208865).
- [67] M.S. Anand, B.M. Pande, R.P. Agarwala, Recovery in neutron irradiated tungsten, *Radiat. Eff.* 39 (1978) 149–155, doi:[10.1080/00337577808234468](https://doi.org/10.1080/00337577808234468).
- [68] Y.-L. Liu, Z.-H. Dai, W.-T. Wang, Influence of carbon-vacancy interaction on carbon and vacancy diffusivity in tungsten, *Comput. Mater. Sci.* 83 (2014) 1–4, doi:[10.1016/j.commatsci.2013.10.034](https://doi.org/10.1016/j.commatsci.2013.10.034).
- [69] V.N. Bykov, G.A. Birzhevoi, M.I. Zakharova, V.A. Solov'ev, Nature and thermal stability of radiation defects in single-crystal tungsten, *Sov. At. Energy* 33 (1972) 930–935, doi:[10.1007/BF01666749](https://doi.org/10.1007/BF01666749).
- [70] L. Ventelon, F. Willaime, C.-C. Fu, M. Heran, I. Ginoux, Ab initio investigation of radiation defects in tungsten: structure of self-interstitials and specificity of di-vacancies compared to other bcc transition metals, *J. Nucl. Mater.* 425 (2012) 16–21, doi:[10.1016/j.jnucmat.2011.08.024](https://doi.org/10.1016/j.jnucmat.2011.08.024).
- [71] C. Becquart, C. Domain, U. Sarkar, A. DeBacker, M. Hou, Microstructural evolution of irradiated tungsten: ab initio parameterisation of an OKMC model, *J. Nucl. Mater.* 403 (2010) 75–88, doi:[10.1016/j.jnucmat.2010.06.003](https://doi.org/10.1016/j.jnucmat.2010.06.003).
- [72] X. Yi, M.L. Jenkins, M.A. Kirk, Z. Zhou, S.G. Roberts, In-situ TEM studies of 150 keV W⁺ ion irradiated W and W-alloys: damage, *Acta Mater.* 112 (2016) 105–120, doi:[10.1016/j.actamat.2016.03.051](https://doi.org/10.1016/j.actamat.2016.03.051).
- [73] X. Yi, M. Jenkins, M. Briceño, S. Roberts, Z. Zhou, M.A. Kirk, In situ study of self-ion irradiation damage in W and W-5Re at 500 °C, *Philos. Mag.* 93 (2013) 1715–1738, doi:[10.1080/14786435.2012.754110](https://doi.org/10.1080/14786435.2012.754110).
- [74] A.E. Sand, S.L. Dudarev, K. Nordlund, High-energy collision cascades in tungsten: dislocation loops structure and clustering scaling laws, *EPL (Europhysics Letters)* 103 (2013) 46003, doi:[10.1209/0295-5075/103/46003](https://doi.org/10.1209/0295-5075/103/46003).
- [75] K. Arakawa, T. Amino, H. Mori, Direct observation of the coalescence process between nanoscale dislocation loops with different burgers vectors, *Acta Mater.* 59 (2011) 141–145, doi:[10.1016/j.actamat.2010.09.018](https://doi.org/10.1016/j.actamat.2010.09.018).
- [76] B.N. Dutta, B. Dayal, Lattice constants and thermal expansion of palladium and tungsten up to 878 °C by X-ray method, *Phys. Status Solidi (b)* 3 (1963) 2253–2259, doi:[10.1002/psb.19630031207](https://doi.org/10.1002/psb.19630031207).
- [77] K.-D. Rasch, R.W. Siegel, H. Schultz, Quenching and recovery investigations of vacancies in tungsten, *Philos. Mag.* A 41 (1) (1980) 91–117, doi:[10.1080/01418618008241833](https://doi.org/10.1080/01418618008241833).
- [78] S.L. Wen, J.M. Chen, X. Liu, H. Zhu, H.Y. Chang, Z. Huang, M. Pan, Y. Zhao, First-principles study on mono-vacancy self diffusion and recovery in tungsten crystal, *Fusion Eng. Des.* 109–111 (2016) 569–573, doi:[10.1016/j.fusengdes.2016.02.044](https://doi.org/10.1016/j.fusengdes.2016.02.044).
- [79] J.N. Mundy, S.J. Rothman, N.Q. Lam, H.A. Hoff, L.J. Nowicki, Self-diffusion in tungsten, *Phys. Rev. B* 18 (1978) 6566–6575, doi:[10.1103/PhysRevB.18.6566](https://doi.org/10.1103/PhysRevB.18.6566).
- [80] A. Hollingsworth, M.-F. Barthe, M.Y. Lavrentiev, P.M. Derlet, S.L. Dudarev, D.R. Mason, Z. Hu, P. Desgardin, J. Hess, S. Davies, B. Thomas, H. Salter, E.F.J. Shelton, K. Heinola, K. Mizohata, A. De Backer, A. Baron-Wiechec, I. Jepu, Y. Zayachuk, A. Widdowson, E. Meslin, A. Morellec, Comparative study of deuterium retention and vacancy content of self-ion irradiated tungsten, *J. Nucl. Mater.* 558 (2022) 153373, doi:[10.1016/j.jnucmat.2021.153373](https://doi.org/10.1016/j.jnucmat.2021.153373).
- [81] D.R. Mason, F. Granberg, M. Boleininger, T. Schwarz-Selinger, K. Nordlund, S.L. Dudarev, Parameter-free quantitative simulation of high-dose microstructure and hydrogen retention in ion-irradiated tungsten, *Phys. Rev. Mater.* 5 (2021) 095403, doi:[10.1103/PhysRevMaterials.5.095403](https://doi.org/10.1103/PhysRevMaterials.5.095403).
- [82] A.R. Allnatt, A.B. Lidiard, *Atomic Transport in Solids*, Cambridge University Press, Cambridge, England, 1993.
- [83] Y.-L. Liu, H.-B. Zhou, Y. Zhang, G.-H. Lu, G.-N. Luo, Interaction of C with vacancy in W: first-principles study, *Comput. Mater. Sci.* 50 (2011) 3213–3217, doi:[10.1016/j.commatsci.2011.06.003](https://doi.org/10.1016/j.commatsci.2011.06.003).
- [84] Q. Yuan, A. Chauhan, E. Gaganidze, J. Aktaa, Direct observation of dislocation loops shrinkage upon annealing neutron-irradiated Fe–9Cr alloy, *J. Nucl. Mater.* 542 (2020) 152401, doi:[10.1016/j.jnucmat.2020.152401](https://doi.org/10.1016/j.jnucmat.2020.152401).
- [85] B.L. Eyre, D.M. Maher, Neutron irradiation damage in molybdenum, *Philos. Mag.* 24 (1971) 767–797, doi:[10.1080/14786437108217049](https://doi.org/10.1080/14786437108217049).
- [86] F. Kroupa, J. Silcox, M.J. Whelan, On the annealing of prismatic dislocation loops in aluminum, *Philos. Mag.* 6 (1961) 971–978, doi:[10.1080/14786436108243356](https://doi.org/10.1080/14786436108243356).
- [87] S.L. Dudarev, M.R. Gilbert, K. Arakawa, H. Mori, Z. Yao, M.L. Jenkins, P.M. Derlet, Langevin model for real-time Brownian dynamics of interacting nano-defects in irradiated metals, *Phys. Rev. B* 81 (2010) 224107, doi:[10.1103/PhysRevB.81.224107](https://doi.org/10.1103/PhysRevB.81.224107).
- [88] S.L. Dudarev, K. Arakawa, X. Yi, Z. Yao, M.L. Jenkins, M.R. Gilbert, P.M. Derlet, Spatial ordering of nano-dislocation loops in ion-irradiated materials, *J. Nucl. Mater.* 455 (2014) 16–20, doi:[10.1016/j.jnucmat.2014.02.032](https://doi.org/10.1016/j.jnucmat.2014.02.032).
- [89] L. Bukonte, T. Ahlgren, K. Heinola, Modelling of monovacancy diffusion in W over wide temperature range, *J. Appl. Phys.* 115 (2014) 123504, doi:[10.1063/1.4869497](https://doi.org/10.1063/1.4869497).
- [90] K. Arakawa, K. Ono, M. Isshiki, K. Mimura, M. Uchikoshi, H. Mori, Observation of the one-dimensional diffusion of nanometer-sized dislocation loops, *Science* 318 (5852) (2007) 956–959, doi:[10.1126/science.1145386](https://doi.org/10.1126/science.1145386).
- [91] D.A. Terentyev, L. Malerba, M. Hou, Dimensionality of interstitial cluster motion in bcc-Fe, *Phys. Rev. B* 75 (2007) 104108, doi:[10.1103/PhysRevB.75.104108](https://doi.org/10.1103/PhysRevB.75.104108).
- [92] T. Hamaoka, Y. Satoh, H. Matsui, One-dimensional motion of self-interstitial atom clusters in A533B steel observed using a high-voltage electron microscope, *J. Nucl. Mater.* 399 (2010) 26–31, doi:[10.1016/j.jnucmat.2009.12.014](https://doi.org/10.1016/j.jnucmat.2009.12.014).
- [93] D. Terentyev, N. Anento, A. Serra, V. Jansson, H. Khater, G. Bonny, Interaction of carbon with vacancy and self-interstitial atom clusters in α -iron studied using metallic-covalent interatomic potential, *J. Nucl. Mater.* 408 (2011) 272–284, doi:[10.1016/j.jnucmat.2010.11.053](https://doi.org/10.1016/j.jnucmat.2010.11.053).
- [94] L. Ventelon, B. Lüthi, E. Clouet, L. Provile, B. Legrand, D. Rodney, F. Willaime, Dislocation core reconstruction induced by carbon segregation in bcc iron, *Phys. Rev. B* 91 (2015) 220102, doi:[10.1103/PhysRevB.91.220102](https://doi.org/10.1103/PhysRevB.91.220102).
- [95] D. Caillard, An in situ study of hardening and softening of iron by carbon interstitials, *Acta Mater.* 59 (2011) 4974–4989, doi:[10.1016/j.actamat.2011.04.048](https://doi.org/10.1016/j.actamat.2011.04.048).
- [96] E.A. Little, Void-swelling in irons and ferritic steels: I. Mechanisms of swelling suppression, *J. Nucl. Mater.* 87 (1979) 11–24, doi:[10.1016/0022-3115\(79\)90122-3](https://doi.org/10.1016/0022-3115(79)90122-3).
- [97] D. Terentyev, K. Heinola, A. Bakaev, E.E. Zhurkin, Carbon-vacancy interaction controls lattice damage recovery in iron, *Scr. Mater.* 86 (2014) 9–12, doi:[10.1016/j.scriptamat.2014.04.003](https://doi.org/10.1016/j.scriptamat.2014.04.003).
- [98] P. Hautojärvi, L. Pöllänen, A. Vehanen, J. Yli-Kaupilla, Vacancies and carbon impurities in α -iron: neutron irradiation, *J. Nucl. Mater.* 114 (1983) 250–259, doi:[10.1016/0022-3115\(83\)90264-7](https://doi.org/10.1016/0022-3115(83)90264-7).
- [99] D. Terentyev, I. Martín-Bragado, Evolution of dislocation loops in iron under irradiation: the impact of carbon, *Scr. Mater.* 97 (2015) 5–8, doi:[10.1016/j.scriptamat.2014.10.021](https://doi.org/10.1016/j.scriptamat.2014.10.021).
- [100] J. Diehl, U. Merbold, M. Weller, Information on vacancy migration in α -iron from annealing experiments, *Scr. Metall.* 11 (1977) 811–816, doi:[10.1016/0036-9748\(77\)90080-1](https://doi.org/10.1016/0036-9748(77)90080-1).
- [101] M. Kiritani, H. Takata, K. Moriyama, F.E. Fujita, Mobility of lattice vacancies in iron, *Philos. Mag.* A 40 (1979) 779–802, doi:[10.1080/01418617908234874](https://doi.org/10.1080/01418617908234874).
- [102] M. Onink, C. Brakman, F. Tichelaar, E. Mittemeijer, S. van der Zwaag, J. Root, N. Konyer, The lattice parameters of austenite and ferrite in Fe–C alloys as functions of carbon concentration and temperature, *Scr. Metall. Mater.* 29 (8) (1993) 1011–1016, doi:[10.1016/0956-716X\(93\)90169-5](https://doi.org/10.1016/0956-716X(93)90169-5).
- [103] X. Sha, R.E. Cohen, First-principles thermoelasticity of bcc iron under pressure, *Phys. Rev. B* 74 (2006) 214111, doi:[10.1103/PhysRevB.74.214111](https://doi.org/10.1103/PhysRevB.74.214111).
- [104] L.-E. Lindgren, J.-G. Back, Elastic properties of ferrite and austenite in low alloy steels versus temperature and alloying, *Materialia* 5 (2019) 100193, doi:[10.1016/j.mtla.2018.100193](https://doi.org/10.1016/j.mtla.2018.100193).
- [105] D. Costa, G. Adjanor, C. Becquart, P. Olsson, C. Domain, Vacancy migration energy dependence on local chemical environment in Fe–Cr alloys: a density functional theory study, *J. Nucl. Mater.* 452 (2014) 425–433, doi:[10.1016/j.jnucmat.2014.05.007](https://doi.org/10.1016/j.jnucmat.2014.05.007).

- [106] K. Arakawa, M. Hatanaka, H. Mori, K. Ono, Effects of chromium on the one-dimensional motion of interstitial-type dislocation loops in iron, *J. Nucl. Mater.* 329–333 (2004) 1194–1198, doi:[10.1016/j.jnucmat.2004.04.263](https://doi.org/10.1016/j.jnucmat.2004.04.263).
- [107] D. Brimbal, B. Décamps, A. Barbu, E. Meslin, J. Henry, Dual-beam irradiation of α -iron: heterogeneous bubble formation on dislocation loops, *J. Nucl. Mater.* 418 (2011) 313–315, doi:[10.1016/j.jnucmat.2011.06.048](https://doi.org/10.1016/j.jnucmat.2011.06.048).
- [108] D. Terentyev, N. Anento, A. Serra, C. Ortiz, E. Zhurkin, Interaction of He and He–V clusters with self-interstitials and dislocations defects in bcc Fe, *J. Nucl. Mater.* 458 (2015) 11–21, doi:[10.1016/j.jnucmat.2014.10.093](https://doi.org/10.1016/j.jnucmat.2014.10.093).
- [109] S. Moll, T. Jourdan, H. Lefaix-Jeuland, Direct observation of interstitial dislocation loop coarsening in α -iron, *Phys. Rev. Lett.* 111 (2013) 015503, doi:[10.1103/PhysRevLett.111.015503](https://doi.org/10.1103/PhysRevLett.111.015503).
- [110] B. Burton, M.V. Speight, The coarsening and annihilation kinetics of dislocation loops, *Philos. Mag. A* 53 (1986) 385–402, doi:[10.1080/01418618608242839](https://doi.org/10.1080/01418618608242839).
- [111] E. Gaganidze, H.-C. Schneider, B. Dafferner, J. Aktaa, High-dose neutron irradiation embrittlement of RAFM steels, *J. Nucl. Mater.* 355 (2006) 83–88, doi:[10.1016/j.jnucmat.2006.04.014](https://doi.org/10.1016/j.jnucmat.2006.04.014).
- [112] A. Chauhan, Q. Yuan, C. Dethloff, E. Gaganidze, J. Aktaa, Post-irradiation annealing of neutron-irradiated EUROFER97, *J. Nucl. Mater.* 548 (2021) 152863, doi:[10.1016/j.jnucmat.2021.152863](https://doi.org/10.1016/j.jnucmat.2021.152863).
- [113] J.S. Wróbel, M.R. Zemła, D. Nguyen-Manh, P. Olsson, L. Messina, C. Domain, T. Wejrzanowski, S.L. Dudarev, Elastic dipole tensors and relaxation volumes of point defects in concentrated random magnetic Fe–Cr alloys, *Comput. Mater. Sci.* 194 (2021) 110435, doi:[10.1016/j.commatsci.2021.110435](https://doi.org/10.1016/j.commatsci.2021.110435).
- [114] V.V. Bulatov, W. Cai, *Computer Simulations of Dislocations*, Oxford University Press, Oxford, 2006.
- [115] G. deWit, J.S. Koehler, Interaction of dislocations with an applied stress in anisotropic crystals, *Phys. Rev.* 116 (1959) 1113–1120, doi:[10.1103/PhysRev.116.1113](https://doi.org/10.1103/PhysRev.116.1113).
- [116] Y.N. Osetsky, A. Serra, B.N. Singh, S.I. Golubov, Structure and properties of clusters of self-interstitial atoms in fcc copper and bcc iron, *Philosophical Magazine A* 80 (2000) 2131–2157, doi:[10.1080/01418610008212155](https://doi.org/10.1080/01418610008212155).
- [117] Y.N. Osetsky, D.J. Bacon, A. Serra, B.N. Singh, S.I. Golubov, One-dimensional atomic transport by clusters of self-interstitial atoms in iron and copper, *Philosophical Magazine* 83 (2003) 61–91, doi:[10.1080/0141861021000016793](https://doi.org/10.1080/0141861021000016793).